

Charles University in Prague
Faculty of Mathematics and Physics

MASTER'S THESIS



Zoltán Mics

Nonresonant ionization of atmospherical gases studied by optical pump–terahertz probe spectroscopy

Department of Chemical Physics and Optics

Supervisors: RNDr. Petr Kužel, Dr.,

Prof. RNDr. Petr Malý, DrSc.

Study programme: Physics

Specialization: Optics and Optoelectronics

Acknowledgments

I would like to thank to everybody, without whom this thesis would not have been written. Especially my supervisor, Petr Kužel, for introducing me into the theme, for his patient guidance and support; the members of the Terahertz group for the helpful and friendly atmosphere.

My special thanks belong to Pavel Jungwirth for discussions in chemistry.

Last but not least, I thank to my parents. Without them my university studies would not be possible.

I hereby state that I have written this diploma thesis by myself using only the cited references. I agree with lending of the thesis.

Prague, 21 April 2006

Zoltán Mics

Contents

1	Introduction	3
2	Principles of THz spectroscopy	5
2.1	THz generation	5
2.1.1	Photoconductive antennas	5
2.1.2	Optical rectification	6
2.2	THz detection	9
2.2.1	Photoconductive antennas	9
2.2.2	Free space electrooptic sampling	9
2.3	Various setups in THz spectroscopy	12
2.3.1	Transmission spectroscopy of samples in steady-state	12
2.3.2	Optical pump THz probe spectroscopy	14
3	Experimental setup	18
4	Ionization of gases	23
4.1	Motivation	23
4.2	Recent research of ionized gases using THz spectroscopy	23
4.3	Ionization mechanisms	24
4.4	Interaction of plasma with THz field	27
4.5	Evaluation of the experimental data	29
5	Experimental results and discussion	33
5.1	Probing the photoionization process	33
5.2	Transient dielectric spectra - plasma oscillations	35
5.3	Measurement of the signal peak with variable pump-probe delay	45
5.4	Rotational lines in the spectra	47
6	Summary	51

Title: Nonresonant ionization of atmospherical gases studied by optical pump-terahertz probe spectroscopy

Author: Zoltán Mics

Institute: Institute of Physics, Academy of Sciences of the Czech Republic

Supervisor: RNDr. Petr Kužel, Dr., Prof. RNDr. Petr Malý, DrSc.

Supervisors' e-mail address: kuzelp@fzu.cz, Petr.Maly@mff.cuni.cz

Abstract: This thesis is focused on time-resolved terahertz (THz) spectroscopy of ionized gases. The most common methods of THz generation and detection are described. Equilibrium and non-equilibrium (transient) THz transmission spectroscopy is discussed. Using THz spectroscopy we characterized the properties of electron-ion plasma in atmospheric gases generated by ultrashort laser pulses. We selected oxygen and nitrogen which are the most important gases in the atmosphere. We developed a new methodology to extract the dielectric function of the plasma from the measured data. In the THz dielectric spectra we observed plasma oscillations and determined the density and the scattering rate of the free electrons for various pump intensities. By varying the intensity and the polarization of the pump beam we distinguished between the multiphoton and strong-field mechanisms of ionization. By changing the delay between the pump pulse and the THz pulse we examined the expansion of the plasma.

Keywords: THz spectroscopy, photoionization, plasma, dielectric response, pump-probe

Chapter 1

Introduction

This diploma thesis deals with time-resolved THz spectroscopy of ionized gases. The THz frequency range is commonly associated with the spectral range from about 0.1 to 3 THz (wavelengths from 0.1 to 3 mm). The spectroscopic method was successfully applied to investigation of semiconductors, dielectrics, superconductors and other chemical and biological systems.

The rise of THz spectroscopy was connected with the development of femtosecond laser sources. The most common methods of THz generation use excitation of materials (semiconductors, nonlinear crystals) by femtosecond laser pulses. The excitation leads to ultrafast generation of polarization in the material, thus producing picosecond THz pulses. The detection of THz radiation is phase-sensitive, measuring the electric field of the THz pulse, not just its intensity. It is also gated by laser pulses, allowing to measure the electric-field profile of the THz pulse in the time-domain. This method - time-domain THz spectroscopy - can be extended by adding an optical excitation pulse to the setup, synchronized with THz generation. By this method - time-resolved THz spectroscopy - it is possible study ultrafast dynamics of charges and dipoles after excitation in the far-infrared spectral range.

As THz radiation is very sensitive to free charge carriers, it has been successfully applied to investigation of semiconductors, superconductors and charge transfer in ionized liquids. It was employed also to the research of polar vibrations and bound charges, for example excitons in semiconductors, soft lattice vibrations in dielectrics and solvation dynamics in liquids.

To our knowledge, up to now optical pump-THz probe spectroscopy was not used for investigation of ionized gases. Due to the above mentioned sensitivity to free electrons, time-resolved THz spectroscopy appears to be a useful tool to study the properties of the plasma generated by photoionization of atmospheric gases. By this method we could obtain information about the parameters of the plasma and about its temporal evolution. To interpret

our experiments, it was necessary to develop new methods of evaluation of the measured data. In addition, fingerprints of rotational spectra of products of the photoionization could be also detected in the THz data.

The knowledge of the nonlinear properties and of the dynamics of photoionized air would be useful to understand the propagation of intense laser pulses in the air. Ionization of oxygen also plays a significant role in the upper atmosphere in absorbing the ultraviolet radiation coming from the Sun.

The aim of this work was namely to show that the time-domain THz spectroscopy is a viable tool for the investigation of photoionization processes by probing the nascent electron-ion plasma. We aimed to understand and describe its interaction with the pulsed THz radiation and to map the phenomena which can be observed. We devoted a considerable effort to prepare an experimental protocol for subsequent more extensive investigations.

This work has the following structure. A review of the principles of THz spectroscopy is provided in Chapter 2. Our experimental setup is described in Chapter 3. Chapter 4 describes the photoionization processes in oxygen and nitrogen and the interaction of the pulsed THz radiation with a photoionized gas. The method of our analysis of the experimental data is also introduced and discussed. The experimental results are shown and interpreted in Chapter 5 and the whole work is summarized in Chapter 6.

Chapter 2

Principles of THz spectroscopy

2.1 THz generation

2.1.1 Photoconductive antennas

Using photoconductive antennas is a well established method to generate THz pulses with non-amplified optical ultrafast laser sources. A semiconductor wafer or film with an applied bias voltage is irradiated by an ultra-short laser pulse with photon energy exceeding the bandgap energy to create free carriers. These are accelerated by the applied electric field (see Fig. 2.1). Following the semiconductor material used the free electron lifetime can span roughly from 100 fs to several ns depending on the trapping and recombination mechanisms. Fast changes of the current are connected with the radiation of a picosecond THz pulse into the free space. Its bandwidth is essentially determined by the optical pulse length, the geometry of the antenna, the lifetime and the mobility of free electrons in the semiconductor. Externally biased emitters are often based on radiation damaged silicon-on-sapphire, semi-insulating InP, GaAs or GaAs grown at low temperature.

There are two versions of this method:

- The first emitters were small aperture antennas [1]. In this case the laser pulse is focused between the electrodes which are separated typically by several tens of microns, so that the dipole source is much smaller than the THz wavelengths. This technology allows using relatively low power laser sources (energy per pulse < 1 nJ) and low voltages can be applied to the antenna electrodes (typically tens of volts). On the other hand, the large divergence of the output THz beam requires utilization of hemispherical or hyperhemispherical high-resistivity silicon lenses put in optical contact with the emitter body.

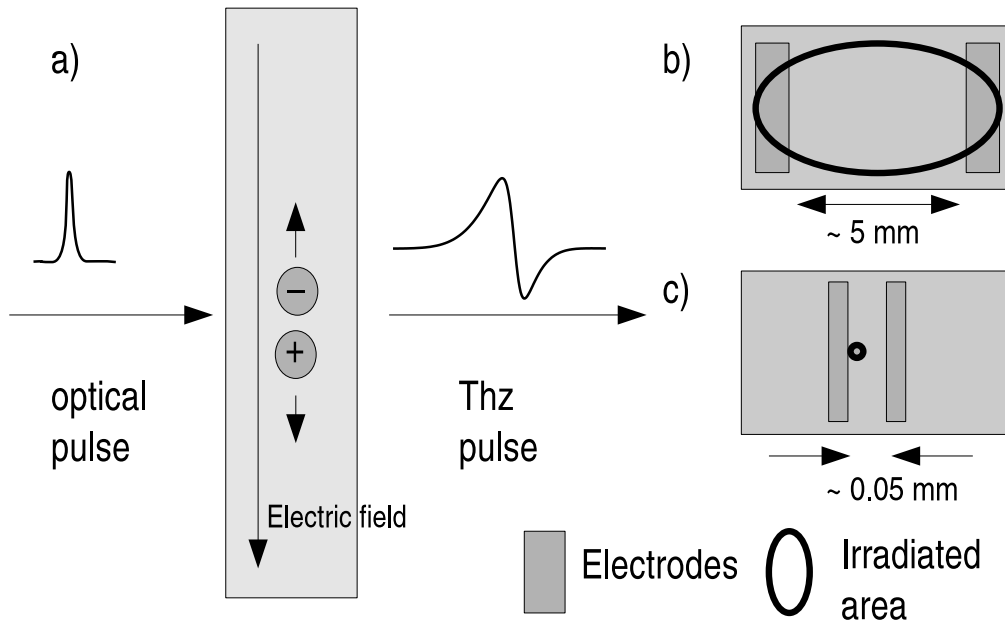


Figure 2.1: (a) Illustration of THz generation by photoconductive antenna. (b) Scheme of large aperture antenna (c) Small aperture antenna

- For large aperture emitters the electrode pads are spaced by several millimeters and a collimated laser beam (it covers the whole gap between the electrodes) is used for photoexcitation. Voltages higher than 1 kV and pulses with > 1 nJ energy are then usually used for an efficient THz generation. These antennas allow generation of intense THz pulses at lower divergence [2].

2.1.2 Optical rectification

Optical rectification is a three-wave mixing nonlinear optical effect, so it can take place only in noncentrosymmetric media. It is a difference frequency generation process, i.e. optical photons with frequencies ω_1 and ω_2 generate a photon with frequency $\Omega = |\omega_1 - \omega_2|$. When a femtosecond laser pulse propagates through the crystal, the mixing of spectral components of the pulse may lead to an efficient generation of far infrared pulses centered near 1 THz. The nonlinear generation process can be described by Maxwell equations, with a second order nonlinear polarization as a source term. Their solution yields the amplitude of each spectral component of the THz pulse

E_T at the output of the crystal [3]:

$$E_T(\Omega) = iL \frac{1}{k(\Omega) + \frac{\Omega}{v_g}} \frac{\Omega^2}{c^2} \chi^{(2)}(\Omega) C(\Omega) \times \exp \left[i \left(k(\Omega) + \frac{\Omega}{v_g} \right) \frac{L}{2} \right] \text{sinc} \left[\left(k(\Omega) - \frac{\Omega}{v_g} \right) \frac{L}{2} \right] \quad (2.1.1)$$

where L is the thickness of the crystal, $C(\Omega) = \int E_0(\omega) E_0^*(\omega + \Omega) d\omega$ is the Fourier transformation of the intensity profile of the input pulse, v_g is the group velocity of the optical pulse. $\chi^{(2)} \equiv \chi^{(2)}(\Omega, \omega - \frac{\Omega}{2}, \omega + \frac{\Omega}{2})$ is the second-order susceptibility of the medium; $k(\Omega)$ is the wave vector of the THz wave: $k(\Omega) = N(\Omega)\Omega/c$, where $N(\Omega)$ is the complex THz refractive index. It is clear from Eq. 2.1.1 that the spectral contents and the intensity of the radiated field is determined essentially by 3 factors:

1. the spectral width of the correlation function $C(\Omega)$ of the optical excitation pulse (this spectra width is inversely proportional to the pulse length in the time domain)
2. the magnitude of the nonlinear coefficient $\chi^{(2)}$
3. the degree to which the phase matching condition (related to the last term of Eq. 2.1.1) is fulfilled.

Efficient generation of THz radiation by optical rectification was found in several systems:

- Polar semiconductors, where the optical pulse creates free carriers. In this case, the laser pulse is absorbed typically within a few microns. The nonlinear susceptibility is resonantly enhanced by interband transition of the carriers. Consequently, the THz generation is efficient even when the phase-matching condition is not satisfied. THz generation by this method can be achieved using for example GaAs [4, 5], InP and CdTe [6].
- The nonlinear crystal is transparent to the optical radiation, and phase matching condition is satisfied. ZnTe is the most commonly used material to generate THz radiation this way. The spectral range of the generated THz pulse spreads from 0.1 GHz up to 3 THz [7]. It is used also in our laboratory. Using 50 fs pulses with 0.2 mJ pulse energy and 810 nm mean wavelength, THz pulse with maximum electric field ~ 4 kV/cm can be generated. Temporal profile of a typical THz pulse is on Fig. 2.2

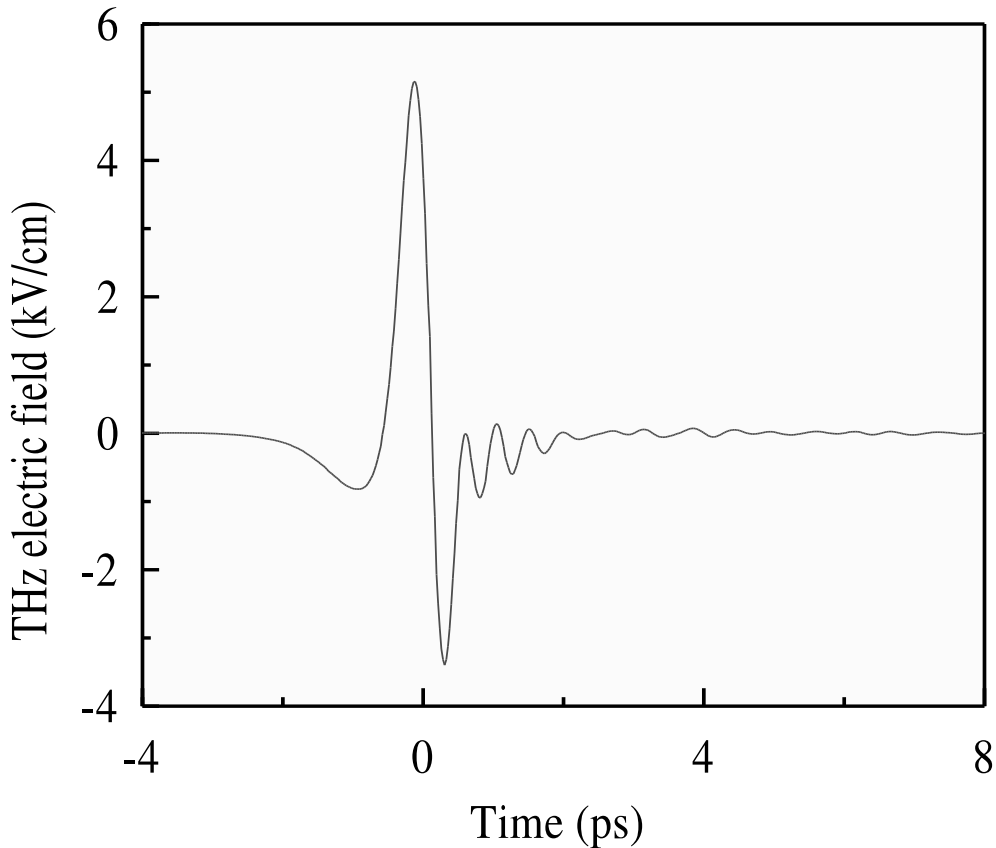


Figure 2.2: A typical THz pulse generated by optical rectification in ZnTe

- Some transparent organic molecular crystals can also efficiently generate THz pulses even if the phase matching condition is not satisfied. They have very high nonlinear susceptibility, because of their high electronic polarizability [8–10]. This is the case of organic ionic salt 4-N,N-dimethylamino-4'-N-methylstilbazolium tosylate (DAST) [9] and -2-(α -methylbenzylamino)-5-nitropyridine (MBANP) [10]. These materials have not yet found widespread use.
- Recently, optical rectification at metal surfaces has been demonstrated as an effective way of THz generation [11, 12]. The second order susceptibility vanishes in the bulk of the centrosymmetric metals, but is non-zero at the surface due to the absence of the inversion symmetry. In this case the response is nonlocal and the nonlinear susceptibility is strongly enhanced by the contribution of the ballistic transport of electrons.

2.2 THz detection

It is possible to conceive gating detection techniques which are sensitive to the electric field of the THz pulse. Using these methods it is possible to reconstruct the time profile of the THz electric field as it propagates through the free space. The Fourier transformation of the measured (time-domain) pulse then provides both amplitude and phase of each spectral component. The phase-sensitivity is an advantage of this method in comparison to classical spectroscopic methods: a complete broadband response function can be obtained from a single measurement without using the Kramers-Kronig relations.

2.2.1 Photoconductive antennas

This mechanism of detection is practically inverse to the THz pulse generation with photoconductive antennas. Here the electric field of the THz pulse plays the role of an external bias. An incident (sampling) laser pulse generates free charge carriers in the semiconductor film or wafer. These carriers are driven by the THz field. If the lifetime of the carriers is very short (compared to the THz pulse duration), the generated current is proportional to the instantaneous THz field coinciding with the optical pulse. By changing the point of coincidence of the THz pulse with the sampling pulse (by means of a moveable delay line) the whole time profile of the THz pulse can be measured [13]. The first phase-sensitive detector for the THz range was based on this mechanism [1]. Low-temperature grown GaAs [14], semi-insulating GaAs [15,16] and semi-insulating InP [15] are the most often used materials for the receiver antenna.

2.2.2 Free space electrooptic sampling

This method is based on the Pockels electrooptic effect. The sensor is a crystal with second order (electrooptic) nonlinearity. The electric field of the THz pulse induces in the sensor a time-dependent birefringence, which practically follows its profile. The birefringence is probed by a polarized optical pulse with a variable delay. The most frequently used sensor is a (110)-oriented ZnTe crystal (generally ZnTe - noncentrosymmetric cubic crystal). A typical setup is in Fig. 2.3. The THz pulse is polarized linearly in the (110) direction. The induced indicatrix projected to the input face of the crystal is in Fig. 2.4 It is rotated by 45° with respect to the horizontal and vertical axes.

Within the simplest model of the sensing process and assuming, that the

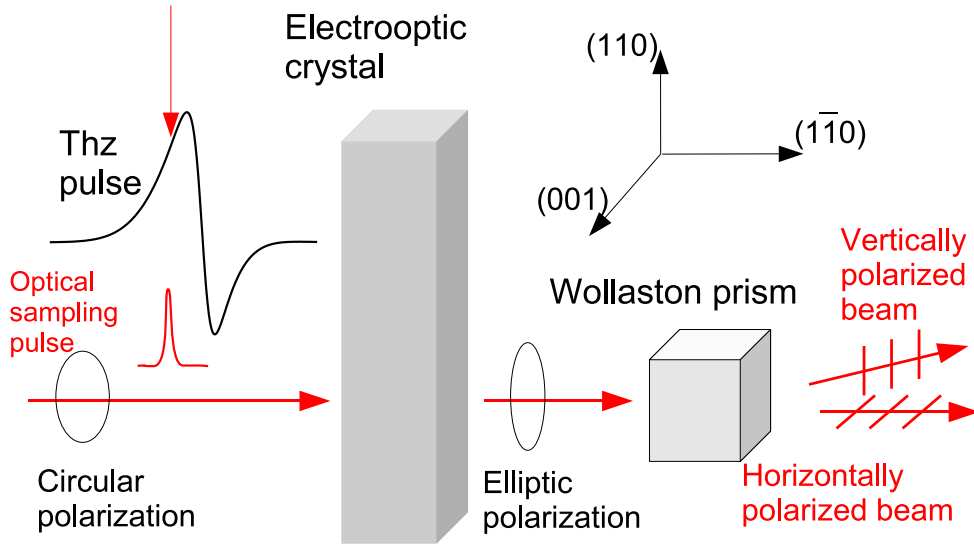


Figure 2.3: Illustration of free space electrooptic sampling

birefringence of the crystal is weak:

$$\Delta n = n_1 - n_2 \propto E_{THz} \quad (2.2.1)$$

The optical sampling pulse is circularly polarized. During its propagation through the crystal its polarization will change to slightly elliptic. The horizontally and vertically polarized parts are separated by a Wollaston prism; their intensities are measured by a pair of balanced antiparallel photodiodes (see inset in Fig. 2.3). In this arrangement the output signal is proportional to the electric field intensity:

$$\Delta I \propto I_0 \sin \Delta \varphi \approx I_0 \Delta \varphi \quad (2.2.2)$$

where $\Delta \varphi = \frac{\omega}{c} \Delta n L$. L is the thickness of the crystal, ω is the mean frequency of the optical pulse. The advantage of using a circularly polarized sampling pulse is that the measured signal is proportional to the THz field (the linearity is satisfied with a precision better than 1% for 1 mm thick ZnTe crystal for fields below 10 kV/cm) [17]:

$$\Delta I \propto E_{THz} \quad (2.2.3)$$

To understand the sensing process more in detail we need to describe the propagation of both the sampling and the THz pulse in the sensor. One

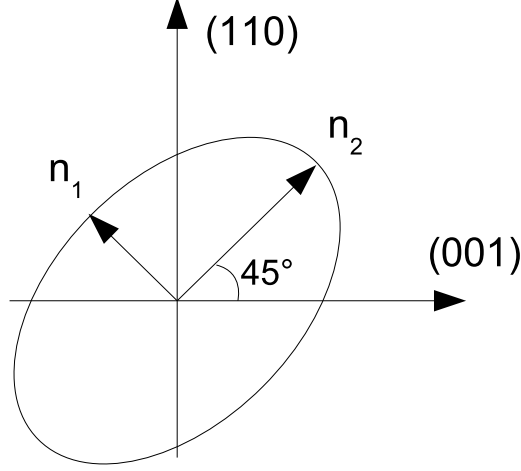


Figure 2.4: The optical indicatrix induced by THz electric field projected to the input face of the crystal

introduces a response function of the sensor [18] $D(t)$ such that:

$$\Delta I(\tau) \propto \int_{-\infty}^{\tau} E_{THz}(t') D(\tau - t') dt' \quad (2.2.4)$$

To evaluate $D(t)$, it is necessary to account for the nonlinear wave-mixing of the sampling and THz radiation in the sensing crystal. It can be shown that the spectrum of the response function of the sensor reads [18]:

$$D(\Omega) \propto \frac{\omega^2}{k(\omega)} \chi_{eff}^{(2)}(\omega; \Omega, \omega - \Omega) C(\Omega) \\ \times L \exp \left[-i \left(k(\Omega) + \frac{\Omega}{v_g} \right) \frac{L}{2} \right] \text{sinc} \left[\left(k(\Omega) - \frac{\Omega}{v_g} \right) \frac{L}{2} \right] \quad (2.2.5)$$

where $\chi_{eff}^{(2)}$ is the effective nonlinear susceptibility of the medium for the given geometrical setup, $E_{THz}(\Omega)$ is the complex amplitude of the THz wave. $C(\Omega)$, L , v_g , $k(\Omega)$, c , are the same as in Eq. 2.1.1. There are three effects that can have crucial effect on the distortion of the measured waveform compared to the true one which is incident on the sensor:

1. The absorption of the nonlinear crystal in the THz range. In the case of ZnTe it is caused by a TO-phonon resonance near frequency 5.3 THz. As a result ZnTe crystal can be used as a THz detector only for frequencies below ~ 4 THz. For higher frequencies, materials such as GaAs and GaP constitute a more suitable choice [19].

2. The optical pulse length related to the spectral width of the function $C(\Omega)$
3. The phase-matching condition. If the phase-matching condition is satisfied, the delay between the THz and the optical pulse remains constant during the propagation through the sensor. Unfortunately, it is rarely possible to achieve the phase-matching condition for the whole bandwidth of the THz pulse. For ZnTe, the phase-matching condition is quite well satisfied for frequencies below 2 THz if sampling pulse at 800 nm is used [19].

Under assumption of an ideal sensing process (i.e. we assume that the phase-matching condition is satisfied and that $C(\Omega)$ is a broad and flat function) we obtain $D(\Omega)$ independent of Ω . Then we can use the simple formulae 2.2.1 and 2.2.3.

2.3 Various setups in THz spectroscopy

THz spectroscopy can be applied to investigation of equilibrium and non-equilibrium (photoexcited) systems. It can determine the dielectric response function of equilibrium systems in the THz frequency range. For nonequilibrium systems, the aim is to obtain the temporal evolution of the dielectric function after photoexcitation.

2.3.1 Transmission spectroscopy of samples in steady-state

This setup is used to determine the steady-state dielectric properties of samples which are sufficiently transparent in the THz range. It is the most often used method in the THz region. It has been applied to study a great variety of materials: dielectrics [20], semiconductors [21], superconductors [22], organic materials [23], liquids [24], gases [25] and flames [26]. The experimental setup is shown in Fig. 2.5. The determination of the dielectric constants of the sample consists in two consecutive measurements:

- measurements of the THz pulse transmitted through the sample
- measurement of a reference waveform obtained when the sample is removed from the beam path (the THz pulse propagates through an empty diaphragm).

The temporal profile of the measured THz field E_{meas} can be expressed as a convolution of a number of terms:

$$E_{meas}(\tau) = E_{emit}(\tau) * P_{bef} * T * P_{aft} * D \quad (2.3.1)$$

$E_{emit}(\tau)$ is the emitted THz field, $P_{bef}(\tau)$ and $P_{aft}(\tau)$ characterize the pulse

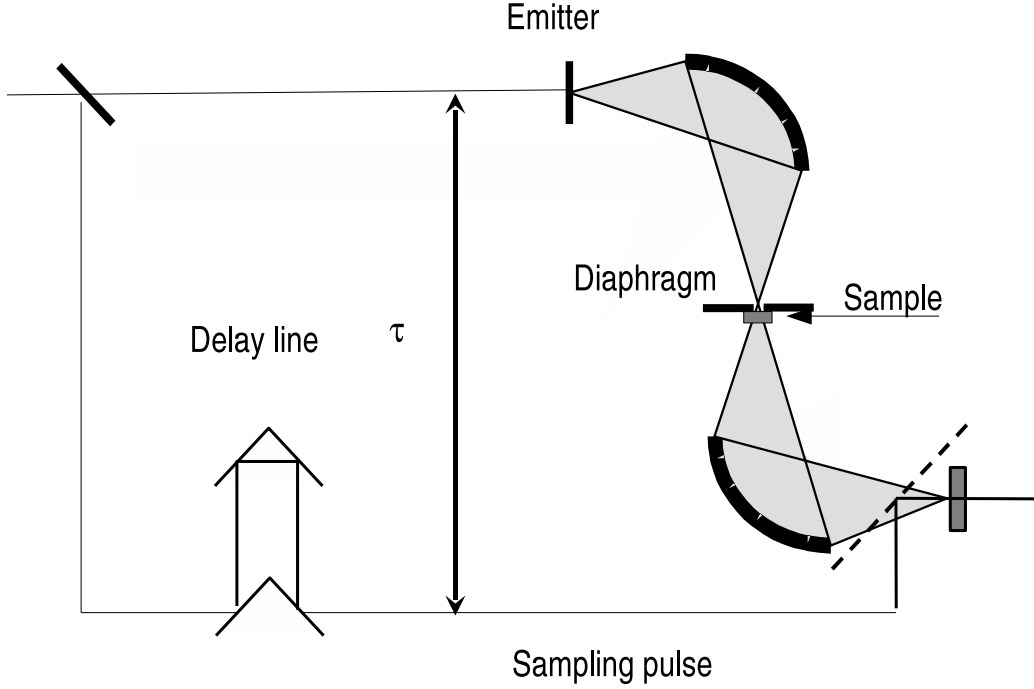


Figure 2.5: Experimental setup for THz transmission spectroscopy

propagation before and after the sample, $D(\tau)$ is the response function of the detector (see Eq. 2.2.5, where $D(\tau)$ is expressed in the Fourier space); $T(\tau)$ is the transmission response function of the sample. The Fourier transform of the waveform gives:

$$E_{meas}(\Omega) = E_{emit}(\Omega) P_{bef}(\Omega) T_{sam}(\Omega) P_{aft}(\Omega) D(\Omega) \quad (2.3.2)$$

where Ω is the THz frequency. It is possible to obtain the transmission function of the sample without the knowledge of the instrumental functions by measuring a reference waveform without a sample. The Fourier transform of the reference waveform gives:

$$E_{ref}(\Omega) = E_{emit}(\Omega) P_{bef}(\Omega) T_{ref}(\Omega) P_{aft}(\Omega) D(\Omega) \quad (2.3.3)$$

So we can obtain the transmission function of the sample:

$$T_{sam}(\Omega) = \frac{E_{meas}(\Omega)}{E_{ref}(\Omega)} T_{ref}(\Omega) \quad (2.3.4)$$

In the most common case the sample is placed in air (or vacuum), so the reference transmission function describes the propagation in free space:

$$T_{ref}(\Omega) = \exp(i\Omega d/c) \quad (2.3.5)$$

Assuming that the THz beam is collimated and the sample is a plane-parallel plate with input face perpendicular to the THz beam, the complex refractive index of the sample is obtained by numerical solution of the complex equation:

$$T_{sam}(\Omega) = \frac{4N}{(N+1)^2} \exp[i\Omega Nd/c] \sum_{k=0}^m \left[\frac{N-1}{N+1} \exp[i\Omega Nd/c] \right]^{2k} \quad (2.3.6)$$

where $N \equiv N(\Omega)$ is the frequency-dependent refractive index of the sample. The first term stands for the Fresnel losses at the input and output face of the sample, the second describes the change of phase (and absorption) in the bulk of the sample. The internal reflections of the THz pulse are accounted for in the summation term.

2.3.2 Optical pump THz probe spectroscopy

The fact that THz spectroscopy uses picosecond THz pulses synchronized with optical pulses, makes it possible to examine the temporal evolution of the sample after optical excitation. If the optical pulse generating the THz radiation and the excitation (pump) pulse are provided by the same source, an optical pump-THz probe experiment can be carried out. The wavelength of the pump beam can be changed by nonlinear conversion. An illustration of this method is in Fig. 2.6. Two independent delay lines can be varied in the experiment: the time τ is connected to the sampling of the THz pulse transmitted through the sample and it has the meaning of the real time; τ_p is the pump-probe delay and characterizes the decay of the sample excitation.

In the case, when the state of the sample changes on time-scale comparable to the temporal length of THz pulse (see Fig. 2.7), it is needed to perform a 2D scan of $E(\tau, \tau_p)$ in order to obtain the maximum information about the system dynamics. It means that THz waveforms have to be measured for different pump-probe delays close enough to have reasonable resolution of the dynamics. However, each part of the THz waveform has different delay

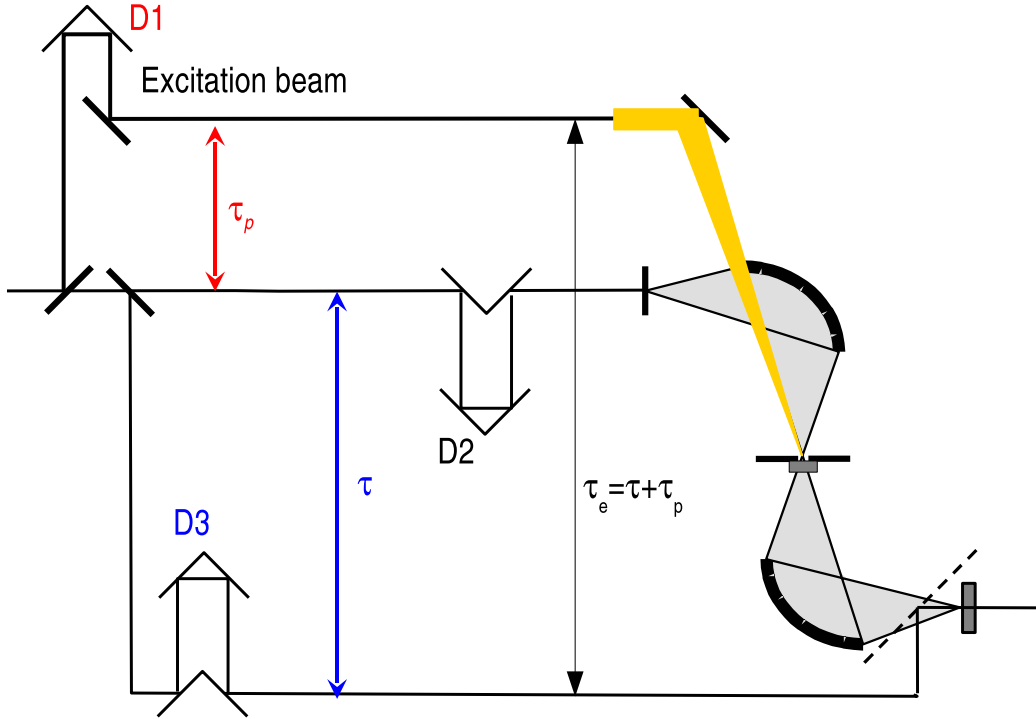


Figure 2.6: Optical pump THz probe experiment

with respect to the time of the excitation. This may lead to complications in analysis of the measured data.

Let us define $T'(t, t') = T(t) + \Delta T(t, t')$ the response function of the photoexcited sample. $T(t)$ is the response function in equilibrium, $\Delta T(t, t')$ represents the change induced by the pump beam. Then the transmitted waveform E_{transm} can be described by expression [27]:

$$E_{transm}(\tau, \tau_p) = \int_{-\infty}^{\tau} E_{THz}(t') T'(\tau - t', \tau_p + t') dt' \quad (2.3.7)$$

where E_{THz} is the field incident on the sample. The equilibrium term can be easily eliminated by measuring a reference waveform, which in this case will be a THz pulse transmitted through unexcited sample (the pump beam is suppressed). The THz field induced by the photoexcitation reads:

$$\Delta E(\tau, \tau_p) = \int_{-\infty}^{\tau} E_{THz}(t') \Delta T(\tau - t', \tau_p + t') dt' \quad (2.3.8)$$

This expression is not a simple convolution, so the transient response function of the sample cannot be extracted by a simple Fourier transformation. The

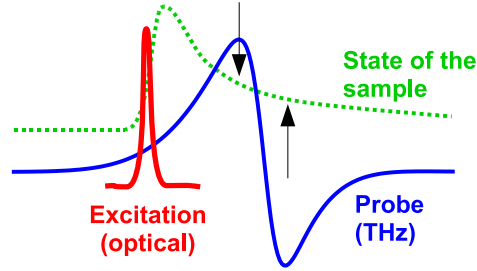


Figure 2.7: Illustration of fast dynamics of a photoexcited system: each point of the THz waveform senses different state in other times after the excitation.

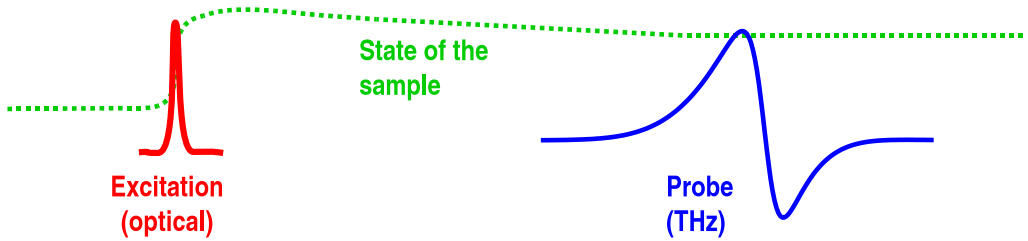


Figure 2.8: Illustration of a system with slow dynamics

problem was solved in [27], by applying 2D Fourier transformation. Anyway, in order to extract meaningful data from the experiment, it is needed to know the instrumental functions of the THz propagation and detection.

In the case of slow dynamics, when the state of the sample does not change significantly during several ps (the THz pulse width - see Fig. 2.8), the evaluation of transmission function induced by photoexcitation can be simplified. It is enough to measure THz transients at several pump-probe delays, and apply a treatment very similar to that applied to the equilibrium THz spectroscopy. In this case Eq. 2.3.8 becomes:

$$\Delta E(\tau, \tau_p) = \int_{-\infty}^{\tau} E_{THz}(t') \Delta T(\tau - t', \tau_p) \quad (2.3.9)$$

This is a true convolution, so by applying Fourier transformation the time-dependent transmission function induced by photoexcitation can be obtained:

$$\Delta t(\Omega, \tau_p) = \frac{\Delta T(\Omega, \tau_p)}{T(\Omega)} = \frac{\Delta E(\Omega, \tau_p)}{E_{ref}(\Omega)} \quad (2.3.10)$$

where $E_{ref}(\Omega)$ is the spectrum of the reference waveform transmitted through the sample in equilibrium (the pump beam is suppressed). From the transmission function, a complex transient dielectric function $\Delta \varepsilon(\Omega, \tau_p)$ can be

obtained either analytically or by a numerical inversion of analytical formulae (this depends on the sample geometry). Our experimental arrangement for THz probing of gas photoionization is very specific. We developed a method tailored for this specific setup allowing us to quantify complex dielectrics spectra of ionized gas. This method will be described in detail in paragraph 4.5.

Chapter 3

Experimental setup

The source of the ultrashort laser pulses is a Ti:sapphire oscillator (Mira seed, Coherent) pumped by laser Verdi. This produces 8 nJ pulses of temporal width 80 fs and repetition rate 76 MHz. These pulses are then amplified in a multipass amplifier (Odin, Quatronics) pumped by laser 527-DP Nd:YLF. At the output we get 1 mJ pulses at 810 nm mean wavelength, 1 kHz repetition rate and 50 fs length.

In our experiments the pulses were divided into two parts by a beamsplitter: up to 80% of the laser power was used for the excitation of the sample, (gas ionization), the remaining part was used for the THz generation and gated detection.

The whole THz setup was enclosed in a box, which was evacuated, then refilled with the examined gas at atmospheric pressure. For the generation and the detection of the THz probe pulse a pair of identical 1 mm thick (110) oriented ZnTe crystals was used. The THz beam was focused by two ellipsoidal mirrors (see Fig. 3.1). A circular aperture with diameter 0.5 mm was placed to their common focal point. In this way up to 90% of the THz signal was blocked by the diaphragm; on the other hand this arrangement allowed us to define more properly the interaction volume of the photoionized gas (see below).

The pump beam was also focused to this pinhole, so that it made an angle of approximately 10° with the THz beam. Note that generally in pump-probe experiments it is recommended to use excitation beam with larger waist than the width of the probing beam. In these conditions, the excitation of the sample can be considered as homogeneous. However, such an arrangement cannot be achieved in our case. On the one hand, the pump beam has to be strongly focused to reach high enough intensities for multiphoton and strong-field ionization processes in the gas; on the other hand, the probing radiation, due to its long wavelength, cannot be focused down to submillimeter spot

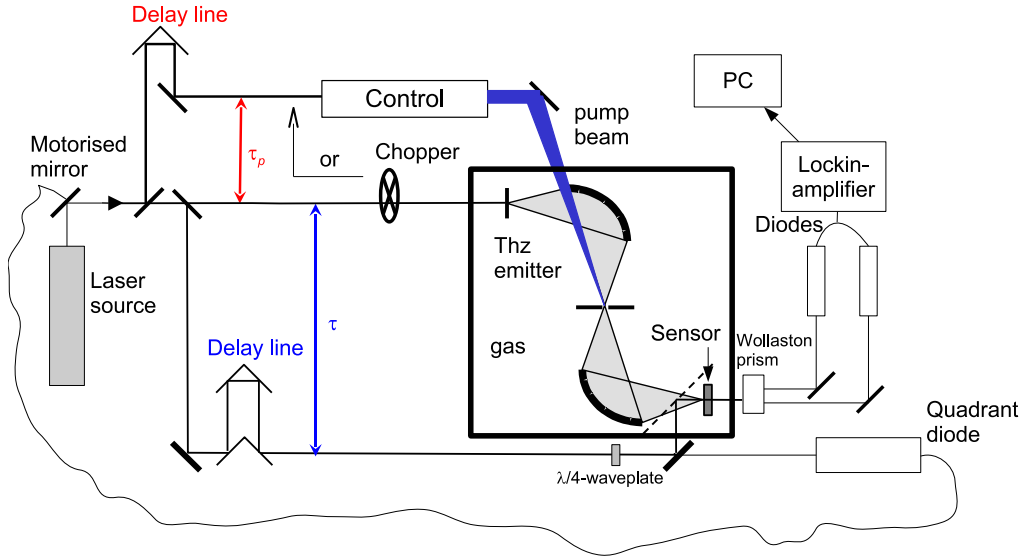


Figure 3.1: Scheme of the experimental setup. The "Control" box represents a specific setup designed for changing the intensity and polarization of the pump beam (in detail, see in Fig. 3.2 for both pump wavelengths used). The chopper is positioned either to the probe (as depicted in the scheme) or to the pump branch.

size. This fact has to be considered during the evaluation and interpretation of the measured data.

We studied the gas ionization using two pump wavelengths: 810 nm and the second harmonic 405 nm. For the second harmonic generation an LBO crystal was used. To distinguish between the possible ionization mechanisms, we examined gas ionized by laser beam with linear and circular polarization. For switching between the two polarization states we used a tunable retardation plate.

The photoionization of O_2 and N_2 at 810 nm and 405 nm are highly nonlinear optical processes. Consequently, the excitation intensity was controlled with a great care. In the case of excitation by blue laser beam, the control of the pump power was possible due to the polarization selectivity of the second harmonic generation. The polarization of the laser pulse incident on the frequency doubler was controlled by a $\lambda/2$ -plate (see Fig. 3.2 a). A control of the orientation of the optical axis of the $\lambda/2$ -plate with respect to the beam polarization (achieved by its rotation around the beam axis) allowed us to vary the blue pump beam intensity by more than an order of magnitude without any other adjustment in the pump branch.

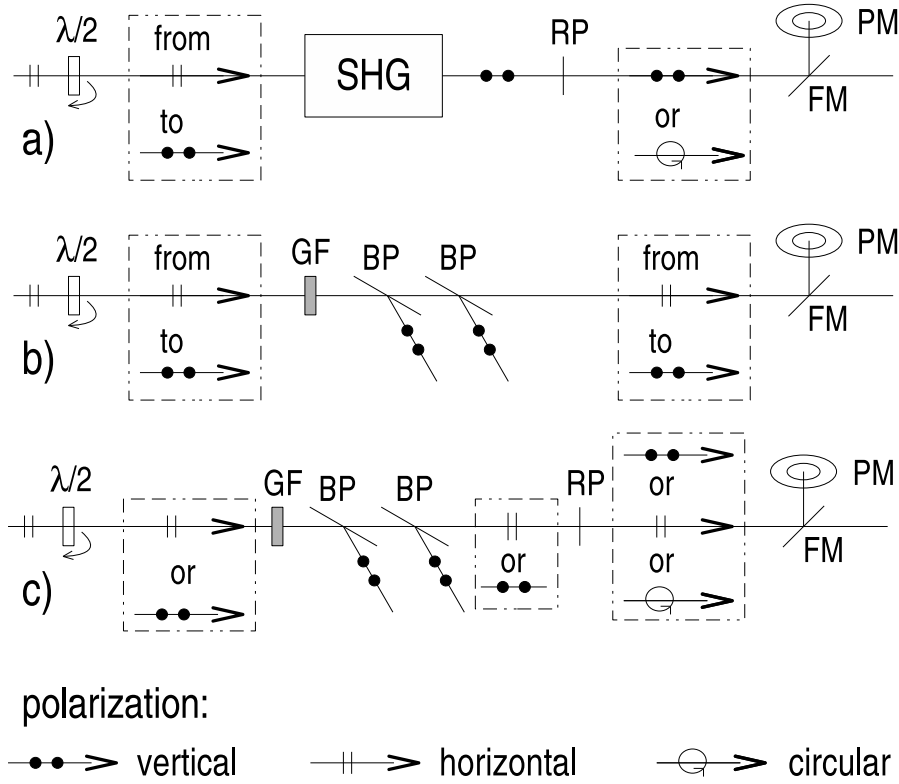


Figure 3.2: Scheme of the pump power control. Pumping with a) 405 nm, linear or circular polarizations; b) 810 nm, linear polarization; c) 810 nm, linear or circular polarizations. $\lambda/2$: half-wave plate, SHG: second-harmonic generation; RP: tunable retardation plate; BP: Brewster plate; GF: thin gray filter; FM: flipping mirror; PM: power meter

For experiments with 810 nm pump wavelength we used the polarization selectivity of the reflection under the Brewster angle (see Fig. 3.2 b). The Brewster plate reflects only light polarized perpendicularly to the plane of incidence (s-polarized light). So in our setup the vertically polarized component of the laser field transmitted through the plates is reduced, while the horizontal component has negligible losses. Consequently, by varying the orientation of the incident laser beam polarization by a $\lambda/2$ -plate it is possible to change the laser intensity. The polarization of the laser beam transmitted through the Brewster plates will be linear with a general orientation. However, this method allowed only a limited control of the pump beam intensity such that the minimum pump power achievable by the $\lambda/2$ -plate rotation was $\sim 50\%$ of maximum power. To reach lower intensities, we used a thin

(0.5 – 1 mm) gray filter for the laser power reduction, assuming that it does not change significantly the pulse length.

A tunable retardation plate (thin Berek compensator) was used to achieve the linear or the circular polarization of the pump beam. The optical axis of this plate was fixed at 45° with respect to the horizontal and vertical beam polarizations. A small tilt of the plate between 0 and $\lambda/4$ retardation position allowed us to switch between linear and circular polarization. Note that for the red pump beam, our setup does not allow continuous tuning of the power of the beam with circular polarization (see Fig. 3.2 c). Only two possible pump powers with circular polarization are available for any grey filter used.

We characterize the pump strength by the peak pulse intensity. The pump beam waist was determined by measuring the intensity profile with a CCD camera at low pump energy. The peak intensity was calculated assuming a Gaussian spatial and temporal profile of the pump pulse. The systematic error in the determination of intensity can be high. We estimate that $\Delta(\log I) \approx \pm 0.3$ (i.e. the pump intensity is comprised between one half and the double of the estimated intensity). On the other hand, random errors within a series of measurements do not exceed 10% of I.

Part of the sampling beam was lead to a quadrant diode, yielding a feedback for a motorized adjustment of a mirror at the output of the amplifier to improve the beam-pointing stability laser beam. In this way, various random effects (temperature variation of the laser sources etc) , which could change the beam path, were eliminated.

A synchronous detection scheme was used locked to a mechanical chopper operated at 166 Hz placed either in the probe branch or in the pump branch. We used the following notation. $E(\tau)$ is the time profile of a THz pulse transmitted through unexcited gas (the pump beam is blocked). $E(\tau, \tau_p)$ is the THz waveform transmitted through photoexcited gas for a pump-probe delay τ_p . The transient waveform defined as $\Delta E(\tau, \tau_p) = E(\tau, \tau_p) - E(\tau)$ reflects the photoinduced changes in the examined gas. It can be measured directly if the chopper is placed into the pump branch.

In the most general case, an acquisition of a two-dimensional transient data $\Delta E(\tau, \tau_p)$ provides full information about the ultrafast infrared dynamics of the system studied (see Sec. 2.3.2). In the present case, experimental results indicate that the transient THz signal varies only very slowly with the pump-probe delay, a significant change starts to show up after a hundred of picoseconds. In this case, it is possible to use Eq. 2.3.10 for the evaluation of the THz transient transmission spectra.

Three kinds of measurements were performed:

- (1) Measurement of the peak values of $\Delta E(\tau, \tau_p)$ with τ fixed at the maximum of the transient signal ΔE_{max} and for selected τ_p (10 ps after photoexcitation). These experiments were performed for both linear and circular polarizations as a function of the pump intensity. These measurements are quite fast, so that it was possible to ensure a very good stability of the laser output during the whole intensity scan. This is important for monitoring highly nonlinear transient signals.
- (2) Measurement of the transient waveform $\Delta E(\tau, \tau_p)$ at selected values of pump-probe delay. By this measurement we access transient spectra of the plasma. In order to extract the plasma characteristics (electron density and scattering time) a reference waveform $E(\tau)$ was always measured.
- (3) Measurement of $\Delta E(\tau, \tau_p)$ with τ fixed at the maximum of the transient waveform and with variable τ_p (pump-probe scans). Such measurements map the plasma decay.

Chapter 4

Ionization of gases

4.1 Motivation

Strong laser pulses have found widespread use in a large variety of applications. For example, they are used for ionization [28], generation of laser pulses on different wavelengths (high harmonics [29], x-ray pulses [30–32]) in rarefied gaseous media, controlled damage [33, 34] and ablation [35, 36] in condensed matter. In all these examples, ionization is either a principle step of the experiment, or it is a side-effect impossible to eliminate. Also plasma generation in the focus of a strong laser pulse directly affects the propagation of the pulse itself, because the properties of the plasma are connected with the intensity of the laser field [37]. So characterizing the evolution of photogenerated plasma would be useful in understanding the above mentioned experiments and phenomena more in detail.

Besides its contribution to laser generated plasmas in the air, photoionized oxygen is of great importance in the upper atmosphere as the source of ozone.

4.2 Recent research of ionized gases using THz spectroscopy

The dynamics of ionized gases at THz frequencies has been studied by two techniques: by analysis of the THz pulse emission from an ionized gas and by THz probing of electron/ion gas plasma.

Löffler et al. reported THz emission from plasma generated by photoionization of electrically biased air. A dc bias voltage of up to 850 V was applied between copper electrodes separated by 0.8 mm from each other. 150 fs laser pulses at wavelength 775 nm with maximum energy of 500 μJ were focused

between the two electrodes. THz generation using these methods is less efficient than from semiconductor antennas or by optical rectification, however, this method could be improved by optimizing the gas pressure or using pulsed high-voltage biasing to reach higher breakdown fields and by choice of better-suited gases [38]. On the other hand there would not be absorption from phonon modes of the transmitter material.

Cook et al. reported generation of THz pulses by four-wave mixing in the air. The nonlinear four-wave mixing of 800 nm pulse of peak intensity $5.10^{14} W/cm^2$ with its second harmonic lead to generation of a THz pulse with peak electric field 2 kV/cm [39]. Kress et al. showed that plasma generation is essential for this type of THz emission [40]. Both the fundamental wave and its second harmonics is required for an efficient THz generation. Note that in our experiments we use either 810 nm or 405 nm pump wavelength and never both at the same time: THz emission by four-wave mixing thus was not possible in our experiments.

Hamster et al. studied THz generation via ponderomotive acceleration of electrons in He plasma by extremely intense laser field. The ponderomotive forces present in the laser focus with peak intensities of $\sim 10^{19} W/cm^2$ lead to ultrafast separation of ions and electrons, thus generating a THz pulse [41,42]. These intensities are by several orders of magnitude higher than those used in our experiments ($10^{13} - 10^{15} W/cm^2$).

Concerning the latter method - THz probing - Jamison et al. [43] studied the dynamics of ionized He gas (pressure 24 mbar) by THz time-domain spectroscopy. The plasma was created by a high voltage pulse power supply, providing $\sim 0.5 kV/cm$ bias field, synchronized with the THz pulses. Varying the delay between the THz probe pulse and the electrical pump pulse the properties of the plasma were probed over several microseconds after ionization, with 30 ps time resolution. The authors determined the time evolution of the free electron density and scattering rate. They obtained electron densities in the range $10^{12} - 10^{13} cm^{-3}$ and scattering times $\sim 10 ps$ for electron kinetic energies of $\sim 5 eV$. The recombination time of electrons with ions was found longer than $1\mu s$.

4.3 Ionization mechanisms

In this work we study the photoionization in two regimes: multiphoton ionization and strong-field tunneling. Multiphoton mechanism consists in ionization by simultaneous absorption of several photons. It can be described by perturbation theory: the laser field represents the perturbation in the hamiltonian describing the matter-light system. Within the tunneling mechanism

the laser ac field changes the Coulomb potential of the atoms and valence electrons can escape through a potential barrier. These mechanisms are quantitatively distinguished by the value of the Keldysh γ parameter [44, 45] (expressed in SI units):

$$\gamma = \omega \sqrt{\frac{E_B}{I}} \sqrt{\frac{m_e}{z_0 e^2}} \quad (4.3.1)$$

E_B is the ionization potential of the atom or molecule, m_e is the electron mass, $z_0 = 377 \Omega$ is the vacuum wave impedance, and e is the electron charge. The multiphoton ionization regime is dominant for $\gamma \gg 1$, the tunnelling for $\gamma \lesssim 1$.

The adiabatic ionization potential of the examined gases [46]:

$$E_B(O_2) = 12.07 \text{ eV} \quad \text{and} \quad E_B(N_2) = 15.60 \text{ eV}$$

For blue light of wavelength 405 nm, which corresponds for photon energy 3.06 eV, 4 photons are required to ionize an oxygen molecule. For nitrogen, energy of 5 photons $5 \times 3.06 = 15.3 \text{ eV}$ is slightly below the required ionization energy, but 5-photon process may be still possible from higher vibrational states of the ground state or in combination with the strong-field tunneling effect. The value of the Keldysh parameter for the highest excitation intensity used at this wavelength ($I = 15 \text{ TW/cm}^2$):

$$\gamma_{blue}(O_2) = 5.1 \quad \text{and} \quad \gamma_{blue}(N_2) = 5.8$$

so multiphoton ionization is expected to be the dominant mechanism of ionization for both gases. Figure 4.1 shows a partial potential-energy diagram for neutral oxygen and nitrogen molecule and for their cations with the ionization pathways expected in our experiment. A resonantly enhanced (3+1)-photon process passing through the Schumann-Runge system $X^3\Sigma_g^- \rightarrow B^3\Sigma_u^-$, which is the strongest absorption band of oxygen, is the most probable [46]. This process also leads to dissociation of oxygen molecules, and subsequently to the formation of ozone. The resonant enhancement via two-photon absorption in the Herzberg band $X^3\Sigma_g^- \rightarrow A^3\Sigma_u^+$ is forbidden due to symmetry. For nitrogen, 5-photon process may be possible, but more probable is a (5+1)-photon process resonantly enhanced passing for example through electronic states $c^1\Pi_u$ or $b'^1\Sigma_u^+$ to $X^2\Sigma_g^+$ (see Fig. 4.1). However, there are many more combinations of possible transitions and we cannot determine the dominating process.

In contrast, with 810 nm pulses (1.53 eV) 8 resp. 11 photons are required to ionize an oxygen, resp. nitrogen molecule. This is a quite improbable

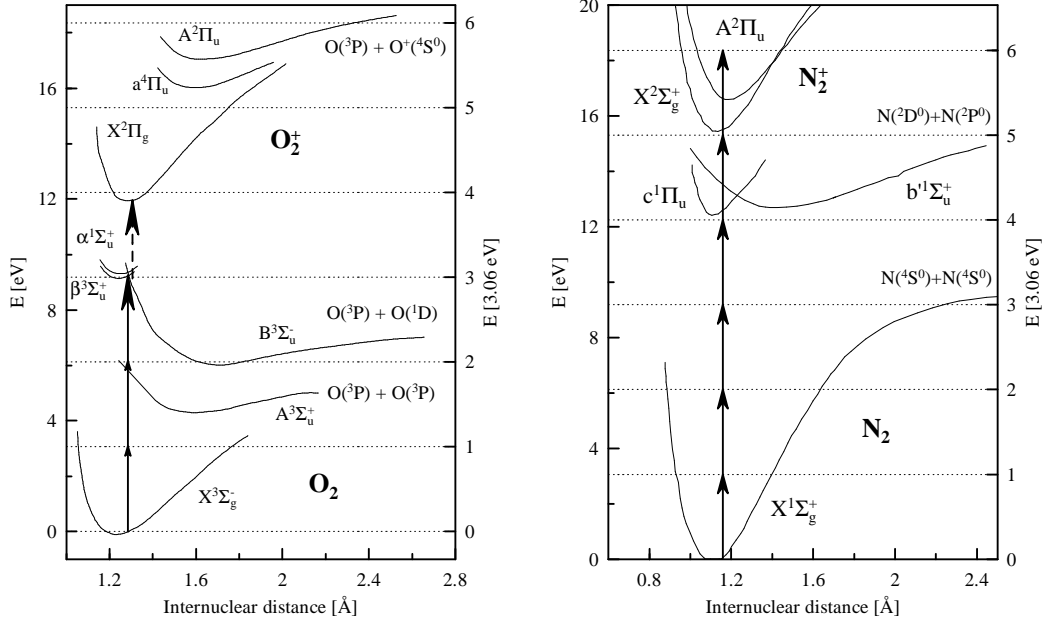


Figure 4.1: Potential-energy diagram displaying the states of oxygen and nitrogen molecule and their cation which are the most important for our experiment. The arrows show the most probable excitation and ionization processes with 405 nm photons.

process for the used pump fields. The Keldysh parameters for the highest pump intensities ($150 \text{ TW}/\text{cm}^2$):

$$\gamma_{red}(O_2) = 0.8 \quad \text{and} \quad \gamma_{red}(N_2) = 0.9$$

In this case the strong-field tunneling is expected to be the dominant ionization regime in the experiments with linearly polarized pump beam. Moreover, for sufficiently high fields the Coulomb potential can be suppressed entirely, so the bound electrons can escape from the attracting field of the ion without tunneling (see Fig. 4.2) [47]. Assuming a quasistatic approximation and considering the effective ionic potential acting on the valence electron $Z = 1$ the threshold intensity leading to the Coulomb barrier suppression can be estimated to be $I_{th} \approx 85 \text{ TW}/\text{cm}^2$ for O_2 and $\approx 240 \text{ TW}/\text{cm}^2$ for N_2 [47].

In contrast, the strong-field effects are expected to be less efficient with excitation by circularly polarized light, which drives the bound electrons on circular orbits [28]. In addition, for small linear molecules like O_2 and N_2 , a rapid molecular alignment with the laser polarization can occur due to the torque on the dipole moment induced by the laser field. This alignment is

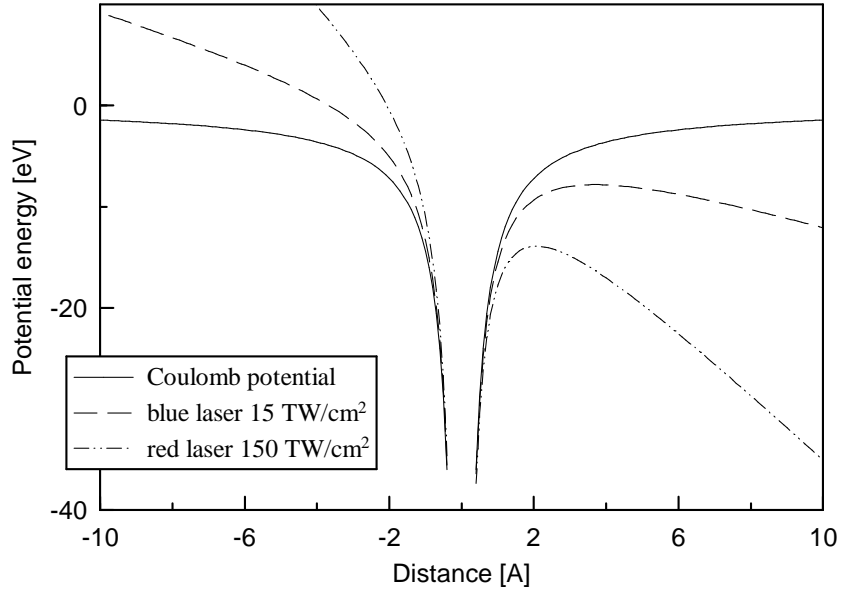


Figure 4.2: Illustration of the tunnelling ionization mechanism in quasistatic approximation - The influence of the laser electric field on the Coulomb potential of the molecule

possible only in linearly polarized light [48]. It was shown by modeling the tunneling ionization that the ionization rate has a maximum when the long axis of the molecular potential axis is parallel with the laser field [49, 50]. From these facts is clear, that comparative measurements by linearly and circularly polarized excitation beams can distinguish between multiphoton and tunneling ionization mechanisms.

4.4 Interaction of plasma with THz field

The THz pulse interacts mainly with free electrons. Interaction with ions can be neglected, because of their greater mass. The dielectric properties of the system can be modeled by the Drude-Lorentz model [51]. The motion of the electrons can be described by equation:

$$\frac{dv(t)}{dt} + \frac{v}{\tau_s} = -\frac{e}{m_e} E_{loc} \quad (4.4.1)$$

where E_{loc} is the local electric field acting on the charges, $v(t)$ is the electron velocity, τ_s the electron scattering time, $-e$ the electron charge, m_e the electron mass. For homogeneous plasma E_{loc} is equal to the THz probe

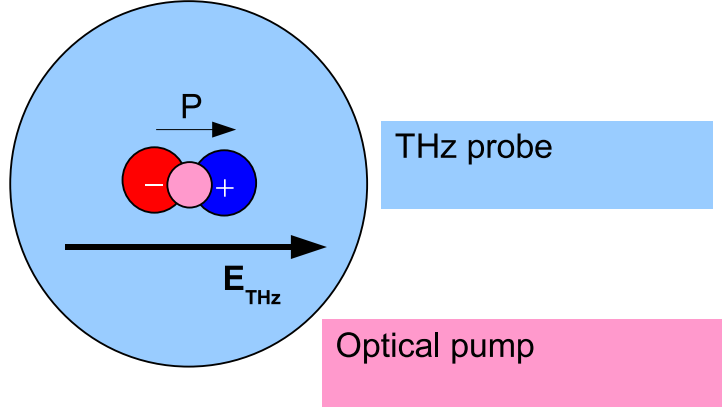


Figure 4.3: Illustration of the charge separation leading to the screening of the THz field

field. Then we obtain the Drude formula for the dielectric function of the plasma [51]:

$$\varepsilon(\Omega) = 1 - \frac{\Omega_p^2}{i\Omega/\tau_s + \Omega^2} \quad (4.4.2)$$

where Ω_p is the plasma frequency connected with the electron density N_e by equation $\Omega_p^2 = N_e e^2 / (\varepsilon_0 m_e)$. However, in our case the excitation beam is narrower than the THz beam, so at early times after photoionization the plasma is localized in a cylinder of much smaller diameter than the waist of the THz beam (see Fig. 4.3). As a result, application of the THz field may lead to a separation of charges. Consequently, we have to account for the polarization P in the plasma induced by the THz electric field which reduces the effective local field E_{loc} :

$$E_{loc} = E_{THz} - \frac{P}{2\varepsilon_0} \quad (4.4.3)$$

where the factor 2 comes from the geometry (cylindrical symmetry) of the system. The rate of change of the polarization is related to the current density:

$$\frac{dP}{dt} = -eN_e v \quad (4.4.4)$$

Then from Eqs. 4.4.1, 4.4.3 and 4.4.4 we get:

$$\varepsilon(\Omega) = 1 - \frac{\Omega_p^2}{i\Omega/\tau_s + \Omega^2 - \Omega_p^2/2} \quad (4.4.5)$$

It can be seen, that the real part of the denominator in Eq. 4.4.5 van-

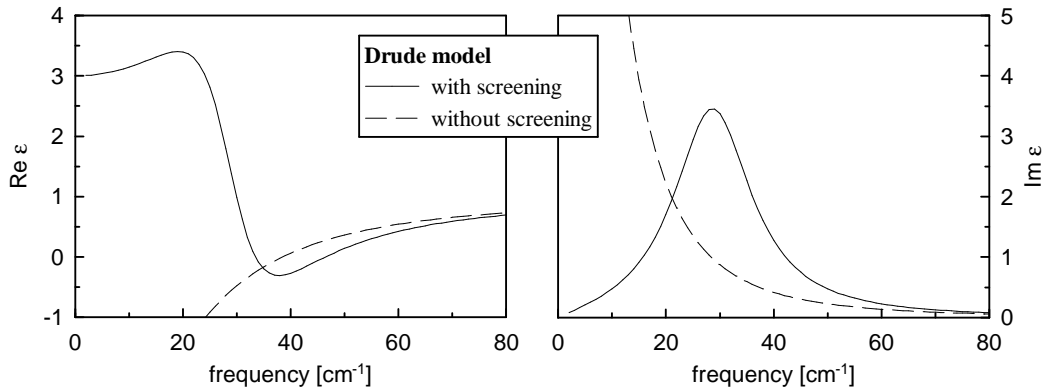


Figure 4.4: Comparison of the simple Drude model with a Drude-Lorentz model accounting for the screening of free carriers. (Computed for $N_e = 2.10^{16} \text{ cm}^{-3}$ and $\tau_s = 300 \text{ fs.}$) The transverse plasma oscillations can be identified at frequency $\Omega_p / (2\sqrt{2}\pi) \approx 28 \text{ cm}^{-1}$.

ishes for $\Omega = \Omega_p / \sqrt{2}$, so for long scattering times τ_s (underdamped plasma) the transverse plasma oscillations can be directly observed at the frequency $\Omega_p / \sqrt{2}$ (see Fig. 4.4).

4.5 Evaluation of the experimental data

From the measured time-domain transient signals we obtain the complex transmission functions $\Delta t(\Omega, \tau_p)$ (see paragraph 2.3.2). These are raw data, from which we need to calculate the dielectric function in order to get more quantitative information about the plasma and the ionized gas. The transmission of the THz beam through the sample is in principle influenced by two phenomena.

- (i) The impedance mismatch at discontinuities and inhomogeneities of the complex refractive index leads to reflection losses (or more generally to scattering losses).
- (ii) The propagation through the sample leads to an exponential attenuation of the wave and to its phase change.

In the following we study the conditions where the contribution due to the impedance mismatch can be neglected and we try to quantify the effective length d_{eff} of the interaction.

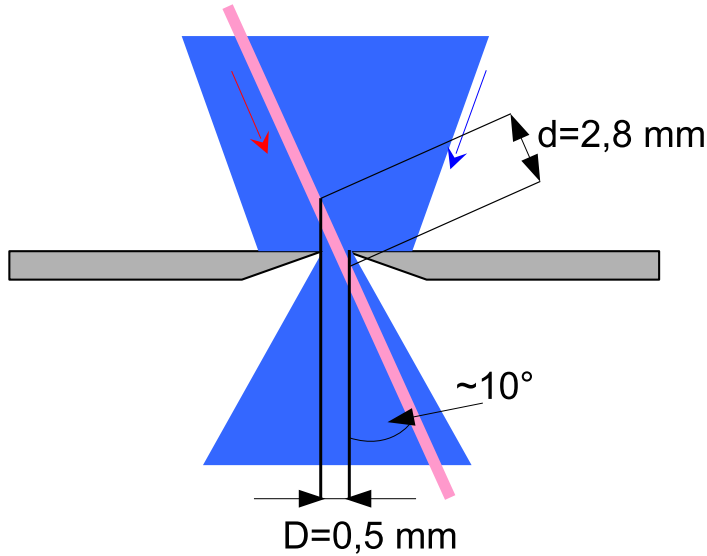


Figure 4.5: Paths of optical and THz beams close to the diaphragm placed to their common focal plane.

The problem of the interaction volume in highly nonlinear optical experiments has been discussed in detail from a general point of view in [45]. More specifically, in our case the interaction volume corresponds to the intersection of a cylinder defined by the pump beam near the focus (note that the Rayleigh confocal parameter of the focused optical beam is $\sim 3 \text{ cm}$) and of a cylinder defined by the diaphragm opening (see Fig. 4.5). Consequently, we assume that our sample can be considered as a 2.8 mm long cylinder with radius r related to the pump beam diameter. However, the intensity profile of the pump beam is approximately Gaussian and the mechanisms of ionization are highly nonlinear. As a result, the plasma is not homogeneous and the estimation of the effective volume and shape is not unambiguous [45]. The main part of the transient signal will come from the central region of the plasma, where the laser intensity reaches the highest values. We expected that from our experiment it would be possible to obtain quantitative results for 405 nm pump wavelength. For this wavelength the radius of the plasma r was determined as follows:

The ionization process is four-photon in O_2 and five-photon in N_2 . Therefore we identify the parameter r with the half-width of the radial profile of I^4 for oxygen and I^5 for nitrogen.

As it was already pointed out, the nonlinearity in experiments with 810 nm pump wavelength is even much higher than that with 405 nm pump. Very high inhomogeneity of the plasma is expected. The experimental results will be analyzed only qualitatively.

Assuming that the approximations above are valid (our sample is homogeneous plasma with clearly defined geometry), we can define a procedure for the evaluation of the data. The volume of the sample is $V = \pi r^2 d$ (d is the length of the cylinder, $d = D/\sin \alpha$). The average path of the THz radiation propagating through this volume is

$$d_{eff} = \frac{\pi r}{2 \sin \alpha} \quad (4.5.1)$$

We transform the cylindric sample to a parallelepiped with an effective thickness d_{eff} and an effective front surface S_{eff} ($= V/d_{eff}$).

Considering this simple arrangement, the transmittance of the probed region consists of two terms:

- One part of the THz beam does not propagate through the ionized volume of the gas. Its transmission function is $t_1 = 1$.
- The other part propagates through the plasma of thickness d_{eff} . The transmission function then reads:

$$t_2(\Omega) = t_F \exp [i\Omega (N - 1) d_{eff}/c] \quad (4.5.2)$$

where $N = n + i\kappa$ is the refractive index of the plasma, t_F accounts for effective transmission losses due to interfaces.

The transmission function of the whole probed region can be obtained from the weighted average of these contributions:

$$t = \frac{t_1 (S_a - S_{eff}) + t_2 S_{eff}}{S_a} \quad (4.5.3)$$

where S_a is the surface of the aperture. The photoinduced change in transmission function then reads:

$$\Delta t = t - 1 = [t_F \exp (i\Omega (N - 1) d_{eff}/c) - 1] \frac{S_{eff}}{S_a} \quad (4.5.4)$$

We assume that the optical constants of the excited gas are very close to the equilibrium values ($n \approx 1$ and $\kappa \approx 0$). The Fresnel transmission coefficient for a homogeneous sample with such properties is very close to unity. One can find $t_F \approx 0.998$ for $\Delta N \approx 0.1$ and $t_F \approx 0.96$ for $\Delta N \approx 0.5$. It

means that the effects caused by the inhomogeneity of the plasma (partial reflections, scattering) are very small comparing to the propagation effects described by the exponential term. So the refractive index can be obtained from transmission function using equation:

$$\Delta t = \{ \exp [i\Omega (N - 1) d_{eff}/c] - 1 \} \frac{8r}{\pi D} \quad (4.5.5)$$

The evaluation of the dielectric function of the plasma is then straightforward:

$$\varepsilon (\Omega) = (N (\Omega))^2 \quad (4.5.6)$$

From the shape of the dielectric function, the electron density and scattering rate can be determined using Eq. 4.4.5.

For the lowest pump intensities, when $\Delta E \ll E$, the exponential term can be developed into Taylor-series. Neglecting the higher terms nonlinear in N , Eq. 4.5.5 can be written:

$$\Delta t = \frac{\Omega}{c} [i(n - 1) - \kappa] \frac{V}{S_a} \quad (4.5.7)$$

So within this approximation the transmission function scales linearly with the interaction volume and $\Delta N = N - 1$.

The evaluation of the optical constants depends to some extent on our choice of the interaction volume, which cannot be unambiguously determined. However, the good agreement of our data with the fits by the Drude-Lorentz model, namely the correct position of the resonance at $\Omega_p/\sqrt{2}$ (see Chapter 5) confirms our choice.

Chapter 5

Experimental results and discussion

In the first two sections of this chapter we present and analyze the results which are obtained at early times after photoionization ($\tau_p = 5 - 10$ ps). In this regime we probe the plasma in a state when processes of the geminate recombination and a possible secondary ionization of molecules by high energy electrons are over. On the other hand, the diffusion of the plasma is in its initial state.

In section 5.3 we briefly analyze the plasma expansion observed when τ_p is increased.

Section 5.4 is devoted to the analysis of specific sharp features observed in the THz spectra which are interpreted as rotational fingerprints of molecular and ionic products of chemical reactions.

5.1 Probing the photoionization process

We examine the photoionization process by measuring ΔE_{max} (i.e. the transient signal $\Delta E(\tau, \tau_p)$ with τ fixed in its maximum and τ_p fixed at 10 ps) with variable pump intensity, for both linearly and circularly polarized pump beams at wavelengths 405 and 810 nm. For better comparison the results are normalized by E_{max} , i.e. the maximum value of the measured reference waveform $E_{ref}(\tau)$.

The measured values of $\Delta E_{max}/E_{max}$ for linear polarization are displayed in Fig. 5.1 for both oxygen and nitrogen.

For blue excitation, in oxygen the peaks follow the simple I^4 rule corresponding to four-photon ionization for pump intensities $I < 4$ TW/cm². Similarly, at pump intensities lower than 17 TW/cm² for nitrogen we get a

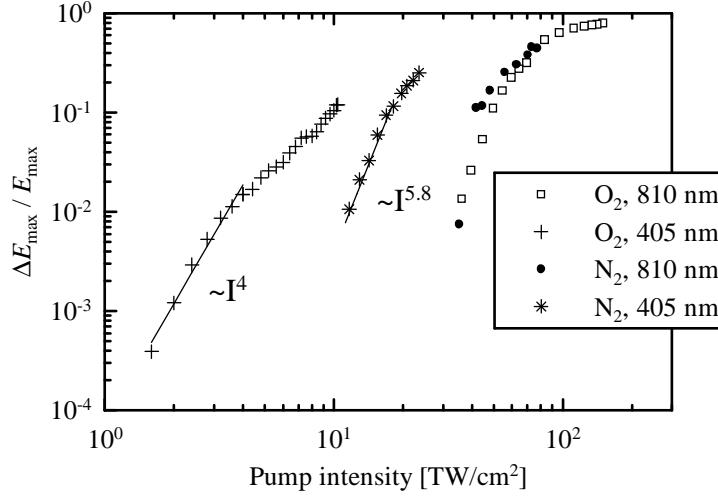


Figure 5.1: Comparison of the measured signal peaks for oxygen and nitrogen, linearly polarized pump beam. For lower pump intensities the peaks are fitted by the simple I^N rule.

$\propto I^{5.8}$ dependence demonstrating a competition between five- and six-photon absorption. Apparently, the six-photon absorption process is the dominant one. For the red pump beam we get comparable signals for nitrogen and oxygen, while for blue pumping the signal peaks are significantly higher for oxygen (see the comparison in Fig. 5.1).

The comparison of signals measured at linearly and circularly polarized pump beams gives us a picture of the dominating ionization mechanisms. The ratios of signals obtained for the two polarization states are displayed in Fig. 5.2 for oxygen and in Fig. 5.3 for nitrogen. For blue pump beam, we get $\Delta E_{circ}/\Delta E_{lin} \approx 0.6 - 0.7$ for oxygen, $\approx 0.4 - 0.5$ for nitrogen. It means that the multiphoton ionization process is dominant, but the contribution of the strong-field tunneling process is not negligible. The slightly lower values obtained for nitrogen may be related to the presence of 5-photon process accompanied with a strong field Coulomb potential renormalization. For the red pump beam, the value of this ratio is ≈ 0.1 for the pump intensities below $65 \text{ TW}/\text{cm}^2$, so strong field ionization is the dominant process.

For higher values of the pump intensity $\Delta E_{circ}/\Delta E_{lin}$ comes closer to one. However, Fig. 5.11 clearly shows, that in this regime $\Delta E_{max}/E_{max}$, which is measured for the linear polarization, tends to one, too. It means that the observed effect for high pump intensities is due to the saturation of the THz absorption rather than to a change of the ionization mechanism.

For oxygen, at $I \approx 75 \text{ TW}/\text{cm}^2$ a dielectric breakdown occurs accom-

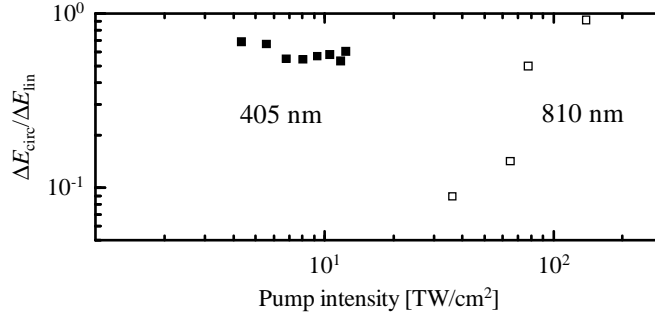


Figure 5.2: The ratio of signal peaks measured for circularly and linearly polarized pump beam for oxygen

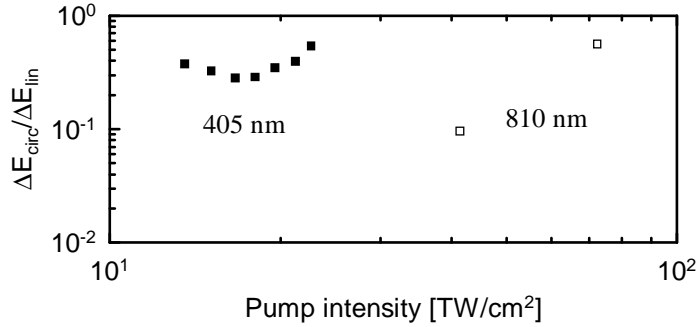


Figure 5.3: The ratio of signal peaks measured for circularly and linearly polarized pump beam for nitrogen

panied by a white-light continuum generation in the focal spot [52]. This threshold intensity is close to intensity $85 \text{ TW}/\text{cm}^2$ needed to suppress the Coulomb barrier of the molecule in a quasistatic limit (see section 4.3). For nitrogen, we did not observe such an effect, as the threshold intensity for Coulomb barrier suppression is $\approx 240 \text{ TW}/\text{cm}^2$ and we use pump intensities lower than $150 \text{ TW}/\text{cm}^2$.

5.2 Transient dielectric spectra - plasma oscillations

It is interesting to make a connection between ΔE_{max} shown in the previous section and the density of free electrons N_e and to make in this way the experimental results more quantitative. This is possible by measuring the

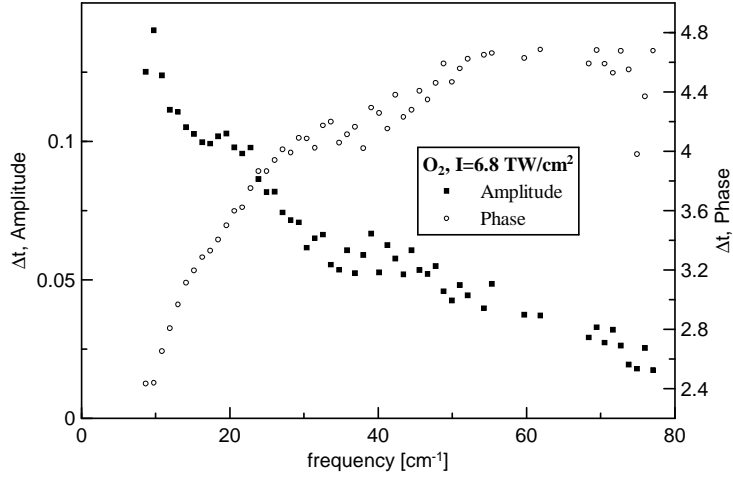


Figure 5.4: Example of a measured transmission function; linearly polarized pump beam at 405 nm

intensity [TW/cm^2]	electron density [$10^{15} cm^{-3}$]	scattering time [fs]
3.2	0.35	320
4.4	0.8	420
5.6	1.7	420
6.8	2.9	370
8.0	3.7	350
10.6	4.7	450

Table 5.1: Fitted plasma parameters for oxygen

transient THz waveforms for several pump intensities and to analyze the transient THz dielectric spectra using the approaches described in sections 4.4 and 4.5.

The transient transmission functions were measured for both oxygen and nitrogen, linearly polarized blue pump beam at pump-probe delay 10 ps. An example of transmission function is in Fig. 5.4. Using equations 4.5.5 and 4.5.6 the dielectric functions were obtained. The results for oxygen are shown in figures 5.5, 5.6, 5.7 and for nitrogen in Figs. 5.8, 5.9. The dielectric functions were fitted by formula 4.4.5. The obtained values of electron densities and scattering times are in tables 5.1 for oxygen and 5.2 for nitrogen. We estimate an error of 20% for electron density and about 50% for scattering time.

It can be seen that oxygen gives a higher signal than nitrogen for comparable pump intensities and that the concentration of free electrons is higher.

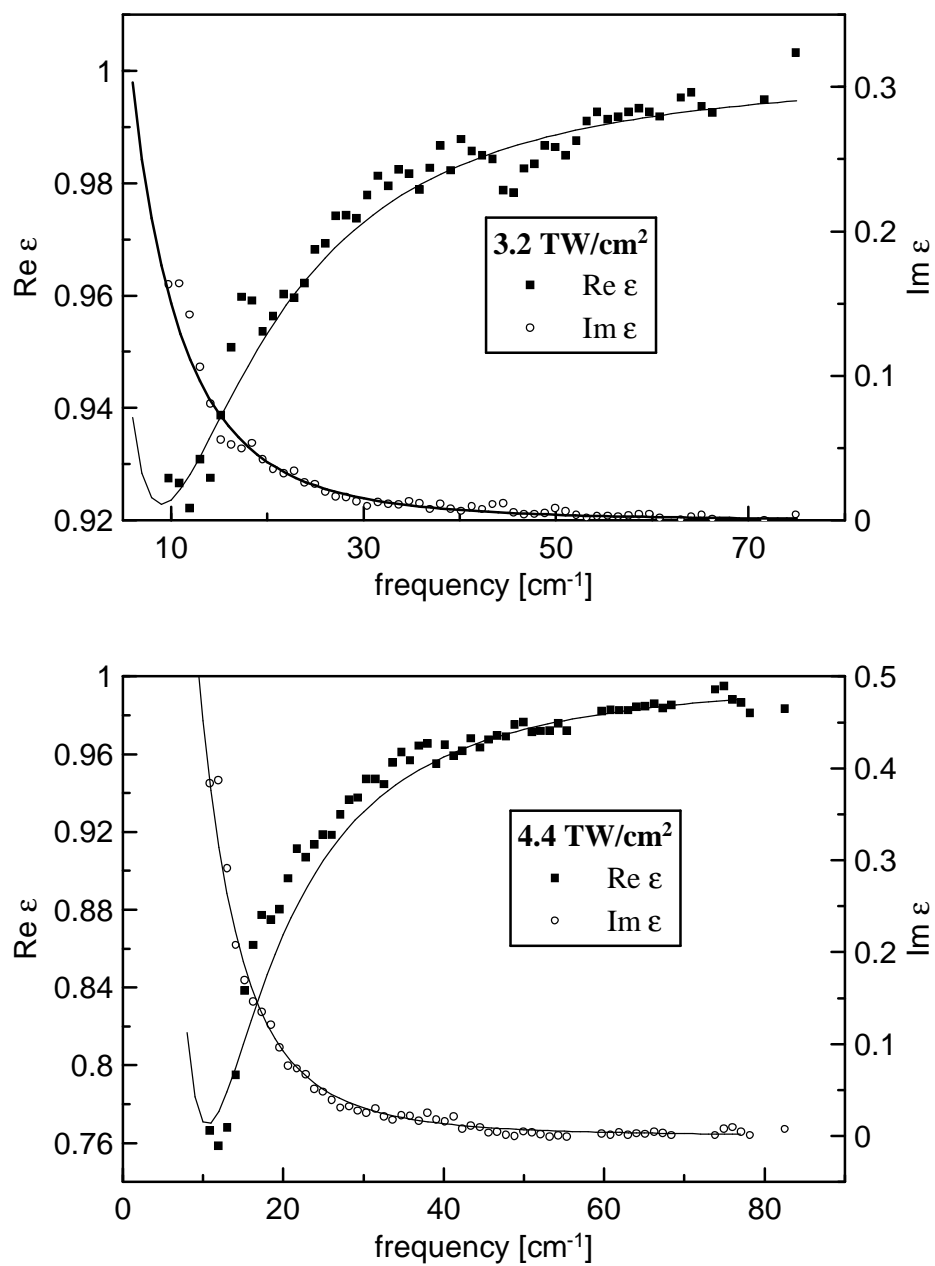


Figure 5.5: The measured dielectric spectra for oxygen fitted by the Drude-Lorentz model (solid lines), first part

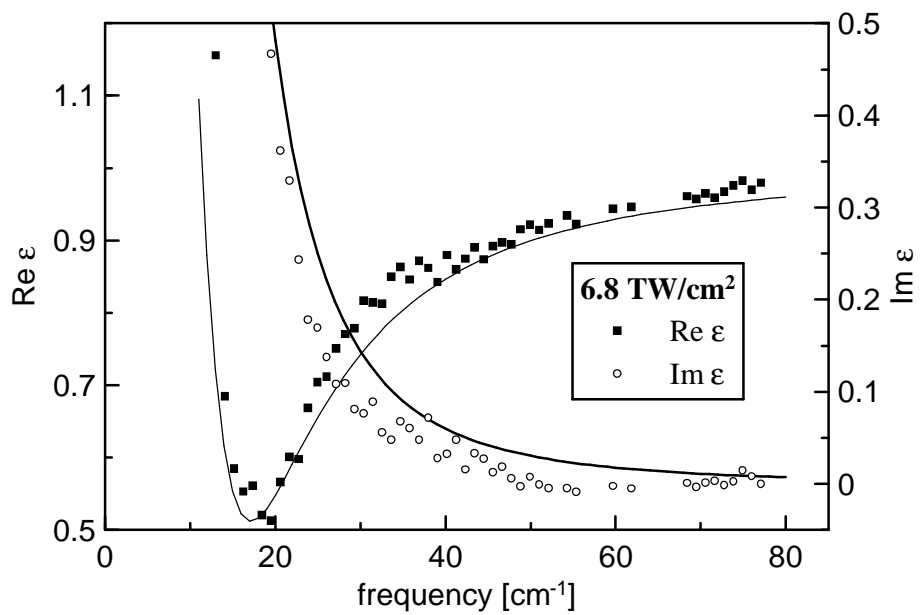
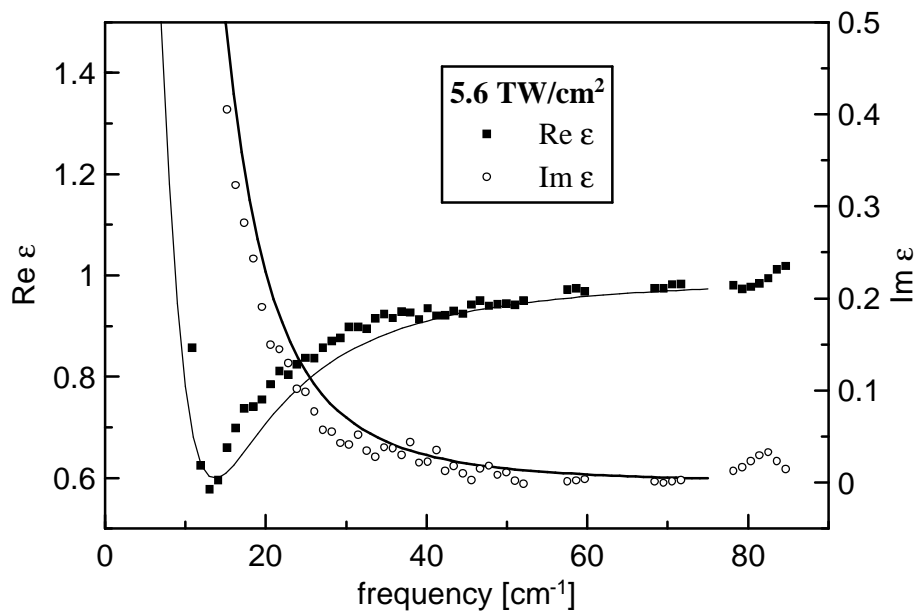


Figure 5.6: The measured dielectric spectra for oxygen fitted by the Drude-Lorentz model (solid lines), second part

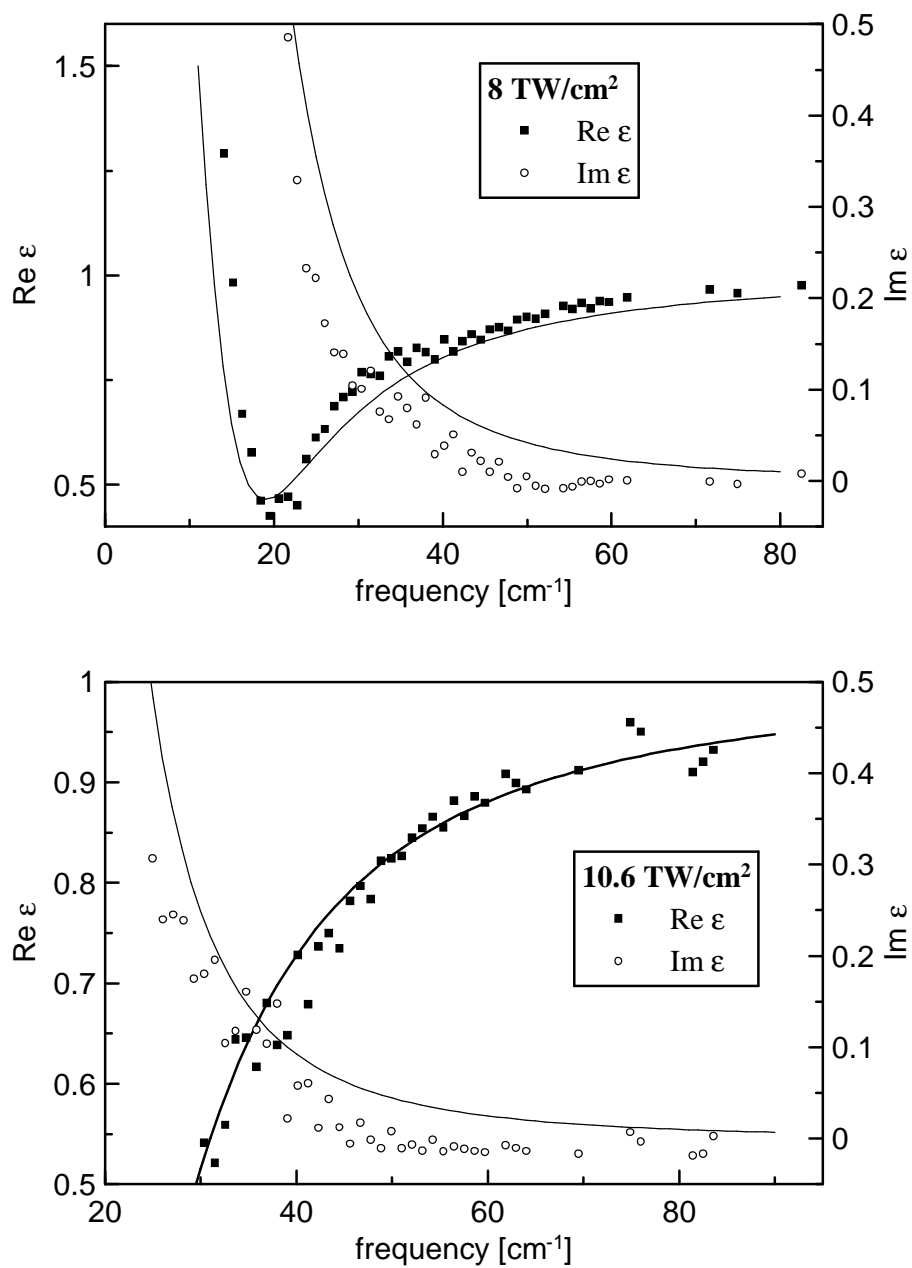


Figure 5.7: The measured dielectric spectra for oxygen fitted by the Drude-Lorentz model (solid lines), third part

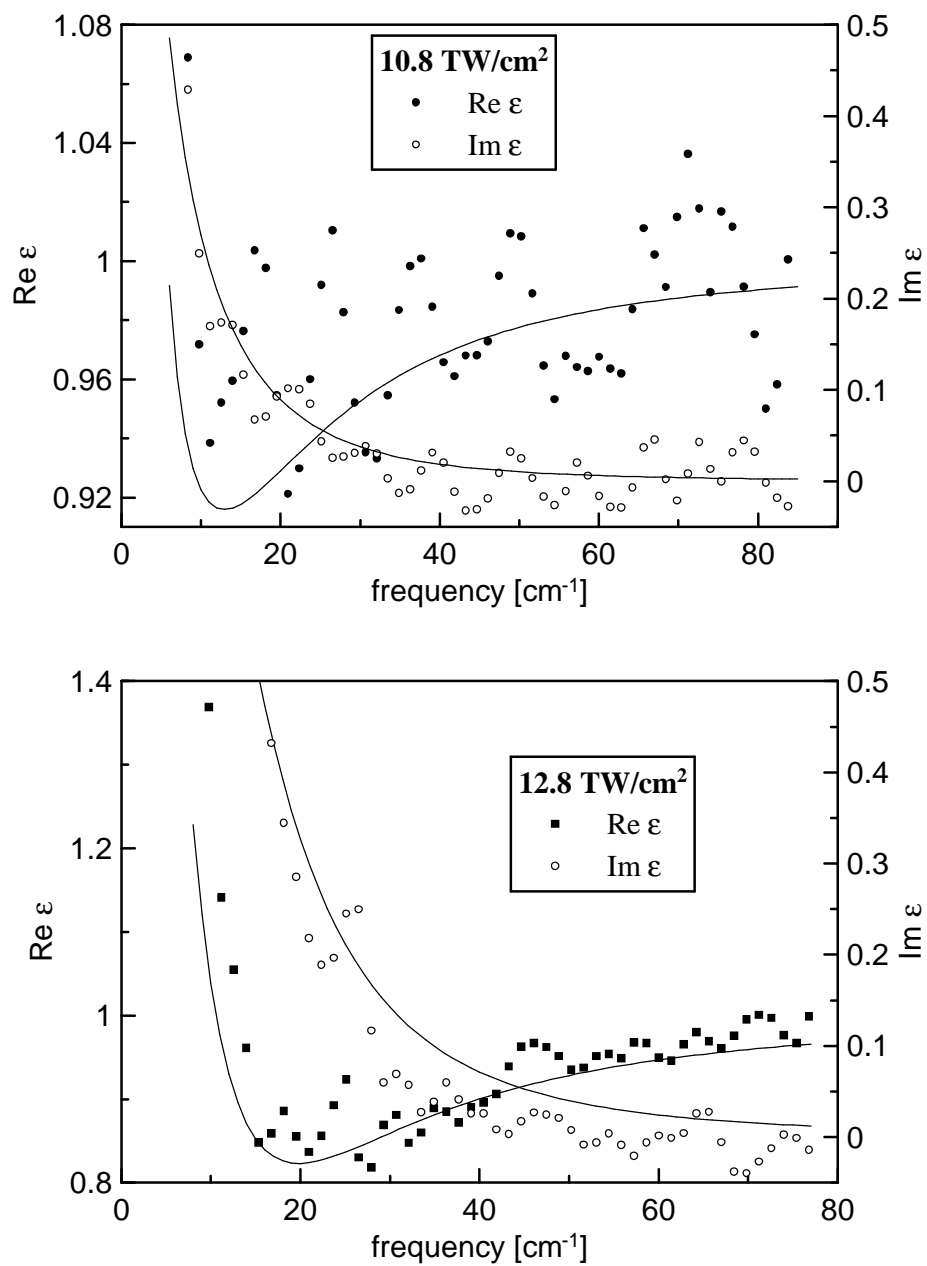


Figure 5.8: The measured dielectric spectra for nitrogen, fitted by the Drude-Lorentz model (solid lines), first part

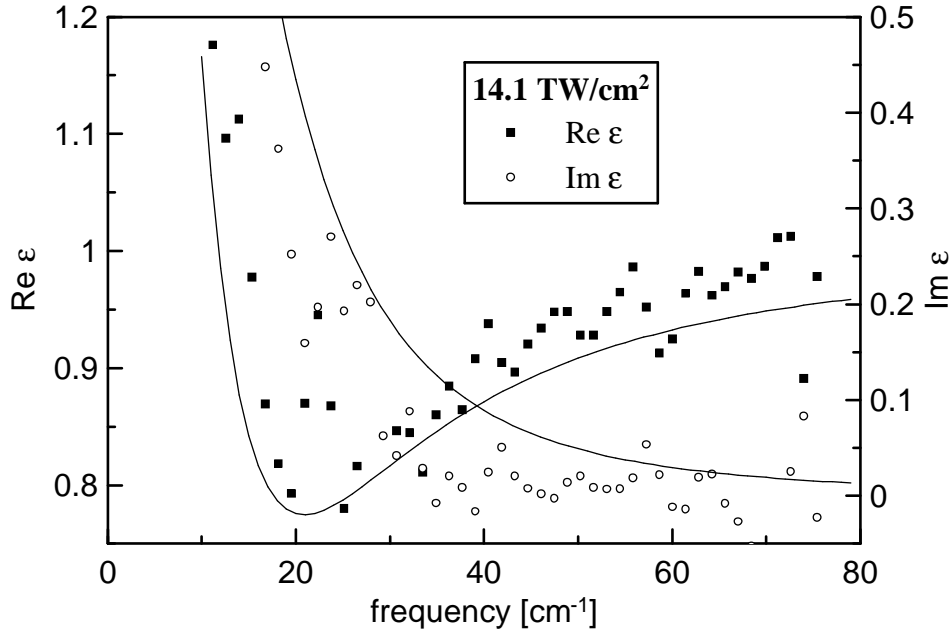


Figure 5.9: The measured dielectric spectra for nitrogen, fitted by the Drude-Lorentz model (solid lines), second part

intensity [TW/cm^2]	electron density [$10^{15} cm^{-3}$]	scattering time [fs]
10.8	0.75	230
12.8	2.5	200
14.1	3.1	210

Table 5.2: Fitted plasma parameters for nitrogen

A comparison of dielectric functions in the two gases for the same pump intensity is displayed in Fig. 5.10.

The transverse plasma oscillations can be directly seen in the dielectric spectra as a steep anomalous dispersion of the real part of the permittivity around frequencies $10 - 30 cm^{-1}$. For higher pump intensities, the concentration of free electrons is higher. As a result, the plasma frequency is higher and the part of $Re \epsilon$ with anomalous dispersion is shifted to higher frequencies. This effect can be seen in Fig. 5.11.

The concentration of the free electrons N_e is well defined by the position of the steep anomalous dispersion of the real part of the permittivity. We checked that the values of the fit parameters do not change significantly if we use slightly different values d_{eff} to get dielectric spectra from the transmission function. To verify the robustness of our analysis and the fit, we

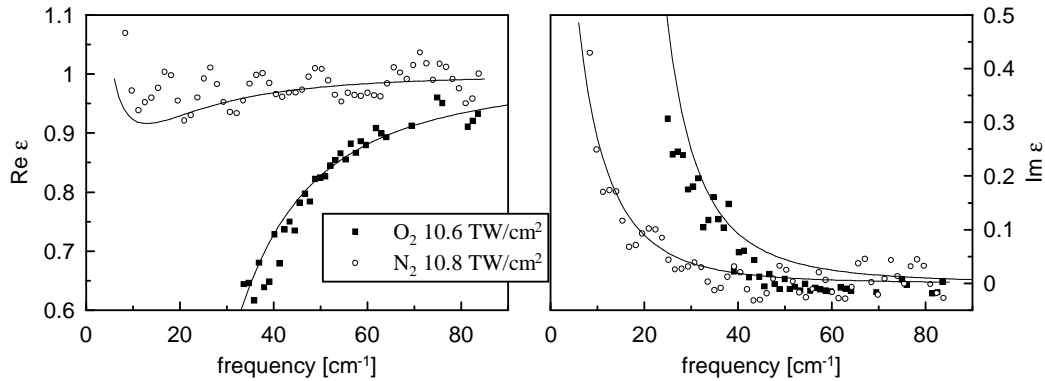


Figure 5.10: Dielectric spectra of nitrogen and oxygen ionized at comparable pump intensities

calculated and fitted trial spectra, where d_{eff} was lowered by about 20%. We found that the values of N_e are practically not influenced by such a change in the data analysis. On the other hand, these changes lead to a slight decrease of the fitted values of the scattering time τ_s (by about 10%). A comparison of two spectra obtained using different values of d_{eff} is displayed in Fig. 5.12.

We performed an additional independent check of the validity of our evaluation of the data. We calculated trial spectra assuming a significantly different interaction volume V of the photoexcited sample: this was achieved by a trial increase of the radius r of the sample cylinder by about 50% in equations 4.5.1 and 4.5.5. The agreement of the fit with the extracted THz dielectric spectra was then significantly lower than that shown in Figs. 5.5, 5.6 and 5.7. In fact, an uncorrect choice of the sample volume leads to a significant change of the behaviour of the high-frequency part of the dielectric function (frequencies higher than 30 cm^{-1}) while the anomalous low-frequency part of the spectra remains practically unchanged. The two parts of the spectra then cannot be satisfactorily fitted by the Drude-Lorentz model.

The values of electron scattering times were found of about 400 fs for oxygen and 200 fs for nitrogen independently on the pump intensity. The concentration of the free electrons is about four orders magnitude smaller than the concentration of neutral molecules. Consequently, the dominant scattering mechanism for free electrons is scattering on neutral molecules [53]. The scattering time can be described by formula:

$$\tau_s = \frac{1}{\sigma N_0 v_e} \quad (5.2.1)$$

where N_0 is the concentration of neutral molecules ($N_0 = 2.7 \times 10^{19} \text{ cm}^{-3}$)

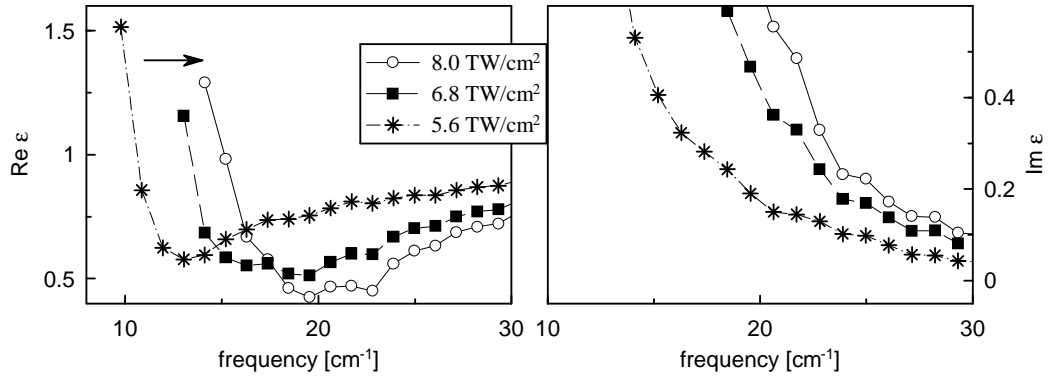


Figure 5.11: Dielectric spectra of oxygen plasma for several pump intensities. The arrow shows the shift of the anomalous part of $Re \epsilon$ to higher frequencies when the intensity of the pump beam is increased.

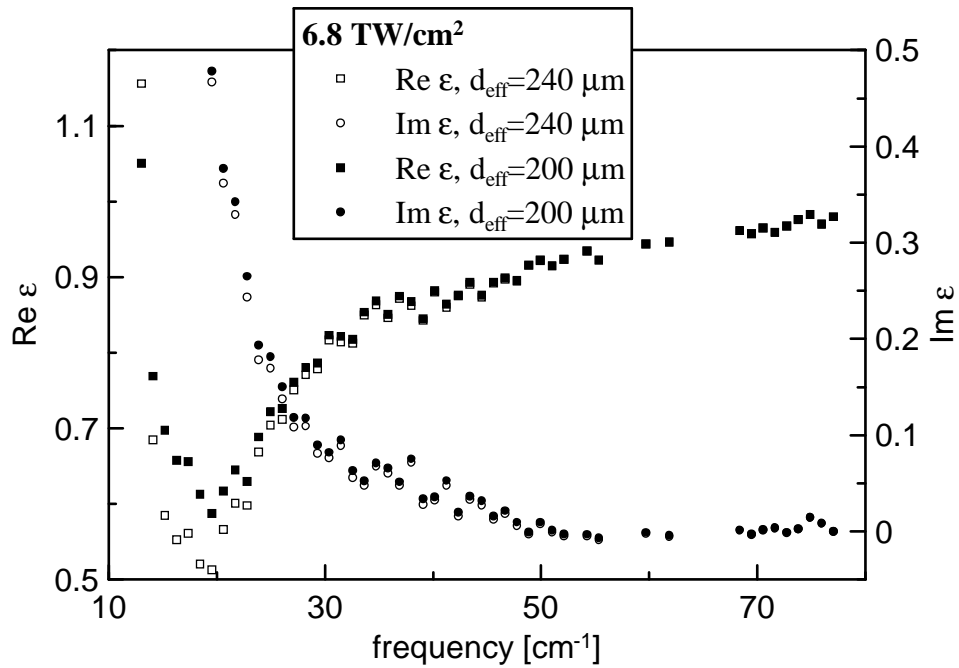


Figure 5.12: Dielectric spectra calculated using different effective values of the sample thickness

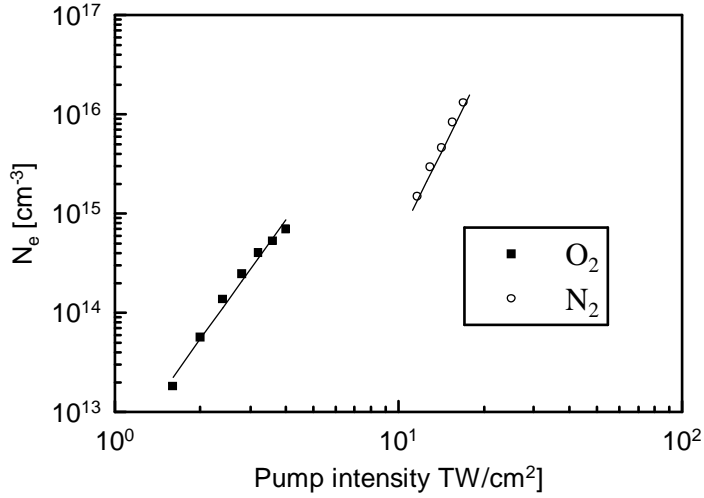


Figure 5.13: Density of free electrons N_e versus the pump intensity for O_2 and N_2 . Pump at 405 nm, linear polarization.

for both oxygen and nitrogen at atmospheric pressure), σ is the electron momentum scattering cross section ($\sigma \approx 10^{-19} \text{cm}^2$ for the given gases [54, 55] and v_e is the thermal velocity of the free electrons. For the measured scattering times we obtain the electron velocity of the order of $v_e \sim 10^6 \text{ m/s}$. This corresponds to kinetic energy of several eV, which can be achieved in our experiments. The scattering time of electrons in ionized nitrogen is two times smaller than the values obtained in oxygen. The reason may be that for nitrogen the sum of the photon energies used in a six-photon absorption process is $6 \times 3.06 = 18.36 \text{ eV}$ and this value exceeds the energy required to ionize the molecule by 2.8 eV, whereas in oxygen $4 \times 3.06 = 12.24 \text{ eV}$ is almost identical to the ionization potential of the oxygen molecule of 12.07 eV. As a result, the generated free electrons in nitrogen acquire higher velocity.

The values of ΔE_{max} measured in the previous section can be connected with the appropriate electron densities obtained in this section determined from the dielectric spectra of the plasma. The results we obtained are shown in Fig. 5.13.

For the red pump beam we could not obtain quantitative results from the analysis of the transient dielectric spectra. In these experiments the plasma is highly inhomogeneous.

- In the radial direction the electron density is proportional in average to I^N , where I is the pump intensity and N is the order of the interaction. The effective volume of the sample is considerably decreased

compared to that considered in the experiments with blue pumping. Consequently, the sensitivity of our experiment is lower and plasma with higher density can only be probed. For such intensities, the approximation leading to Eq. 4.5.5 serving for the transient data analysis becomes questionable.

- The plasma is expected to be highly inhomogeneous even along the pump beam path (i.e. along the axis of our cylindrical sample) when the strong field ionization mechanism is dominant. Hot free electrons with high kinetic energies sufficient for subsequent ionization by collisions may become available. This may lead to an inhomogeneous distribution of free electrons.

5.3 Measurement of the signal peak with variable pump-probe delay

By these measurements we examined the change of the average THz response of the plasma: the delay time τ was fixed to the value ΔE_{\max} for which the transient signal $\Delta E(\tau, \tau_p)$ reaches its maximum and the delay time τ_p was scanned. The measured results are in Fig. 5.14 and 5.15 (for both pump wavelengths). At zero pump-probe delay the signal shows a sharp rise. Over approximately 100 ps after excitation the signal has nearly constant value. This plateau is followed by a decay which can be fitted by an exponential curve with time constant ≈ 400 ps. The same shape of the signal is observed also for lower pump intensities than those reported in Fig. 5.14. Overall, the shape of the signal confirms the application of our approximation of slowly varying dynamics.

We have already pointed out that for low pump intensities the transient THz signal is proportional to the total number of electrons probed by the THz field. It means that for early time delays τ_p where the plateau is observed in the pump-probe scan of ΔE_{\max} this number remains constant. The signal is governed by the diffusion of carriers within the diaphragm clear aperture. The temporal extent of the plateau then corresponds to the time the electrons need to escape from the probed volume.

The origin of the plateau in the pump-probe scans (see Fig. 5.14) for high pump intensities ($I > 4.4$ TW/cm²) can be understood from Fig.5.16, where the transient transmission spectra are shown for 12 TW/cm² pump intensity at several pump-probe delays. Unfortunately, for these intensities the approximations allowing us to calculate the dielectric spectra are no more valid and we can draw some qualitative comments only. At early times after photo-

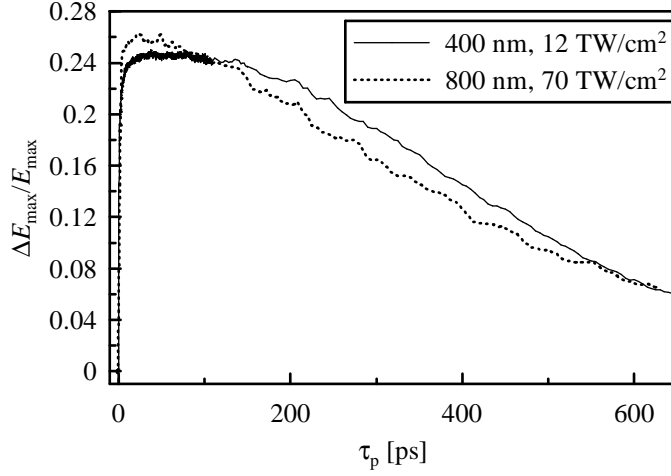


Figure 5.14: The peak THz signal from O_2 depending on the pump-probe delay

ionization, the electron plasma is dense and confined to a rather small volume. In these conditions, the electron plasma density amounts $\approx 10^{16} \text{ cm}^{-3}$ and the plasma frequency $\Omega_p/(2\pi) \approx 30 \text{ cm}^{-1}$. Note that the excitation of the transverse plasma oscillations by the THz field at $\tau_p = 10 \text{ ps}$ is clearly observed as a decrease of the transient transmission around $\Omega_p/(2\sqrt{2}\pi) \approx 21 \text{ cm}^{-1}$ (see Fig. 5.16). Subsequently, a plasma expansion in the radial direction (with respect to the direction of the pump beam propagation) occurs leading to the reduction of the electron density. However, the sample is not in the linear regime described by Eq. 4.5.7. Consequently, the transient spectrum must change its shape. The transverse plasma oscillations are shifted to lower frequency and the high-frequency part of the transient signal is reduced (cf. curves in Fig. 5.16 obtained for 10 and 60 ps pump-probe delay). The total number of probed free electrons being still conserved we come to the conclusion that the volume of the plasma cylinder has significantly increased in the radial direction and, in this regime, the product $N_e d_{\text{eff}}^2$ remains constant.

For the delays higher than 100 ps the free electrons with the highest velocities can reach the boundary of the probed region, i.e. they get out of the clear aperture of the diaphragm and the overall signal decreases. These hypotheses seem to be in qualitative agreement with the results published in [43], where the recombination time of electron plasma in He was found to be larger than several μs .

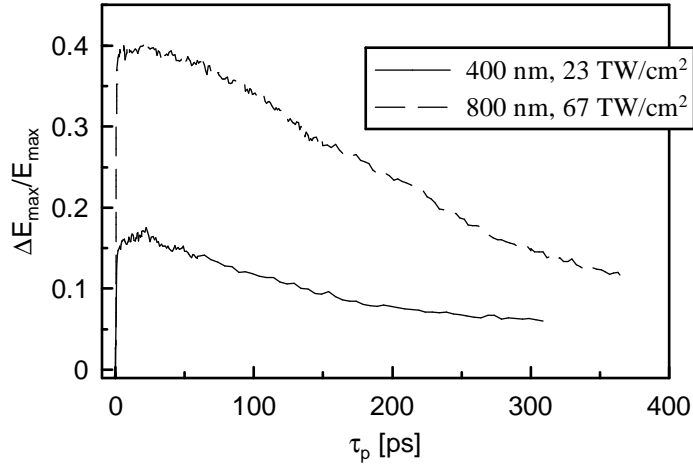


Figure 5.15: Scanning the peak THz signal from N_2 with variable pump-probe delay.

5.4 Rotational lines in the spectra

Ozone rotational spectral lines were detected at frequencies 21.9 and 28 cm^{-1} in the spectra of both reference (pump-beam off) and transient (pump beam on) waveforms in experiments with oxygen (see Fig. 5.17) [46]. This demonstrates pump-induced formation and long-lived presence of ozone in the experimental box. The main source of the ozone are the oxygen atoms created by the dissociation of oxygen molecules (see paragraph 4.3). The formation of ozone is not a transient effect, its presence was detected only after sufficiently long pumping, not immediately after refilling the experimental chamber with fresh oxygen. As the whole path of the THz beam is about 60 cm long, even relatively low concentration of ozone could be detected. In the transient transmission functions (ratio of the transient and reference spectra) these lines are not present.

Rotational lines of residual water vapor were also detected in both transient and equilibrium waveforms (see in Fig. 5.17). We estimate that the ratio of concentrations of water vapor and oxygen was 1:1000.

In contrast to these quasi-equilibrium spectral lines, a marked transient feature is observed near 37 cm^{-1} for the pump intensities higher than 8 TW/cm^2 . This line is observed both in amplitude and phase spectra (see Fig. 5.16); its shape evokes an oscillatory mode with a lifetime exceeding 300 ps. We believe that this line cannot be directly related to the electron plasma dynamics which is as a rule strongly dependent on the free charge

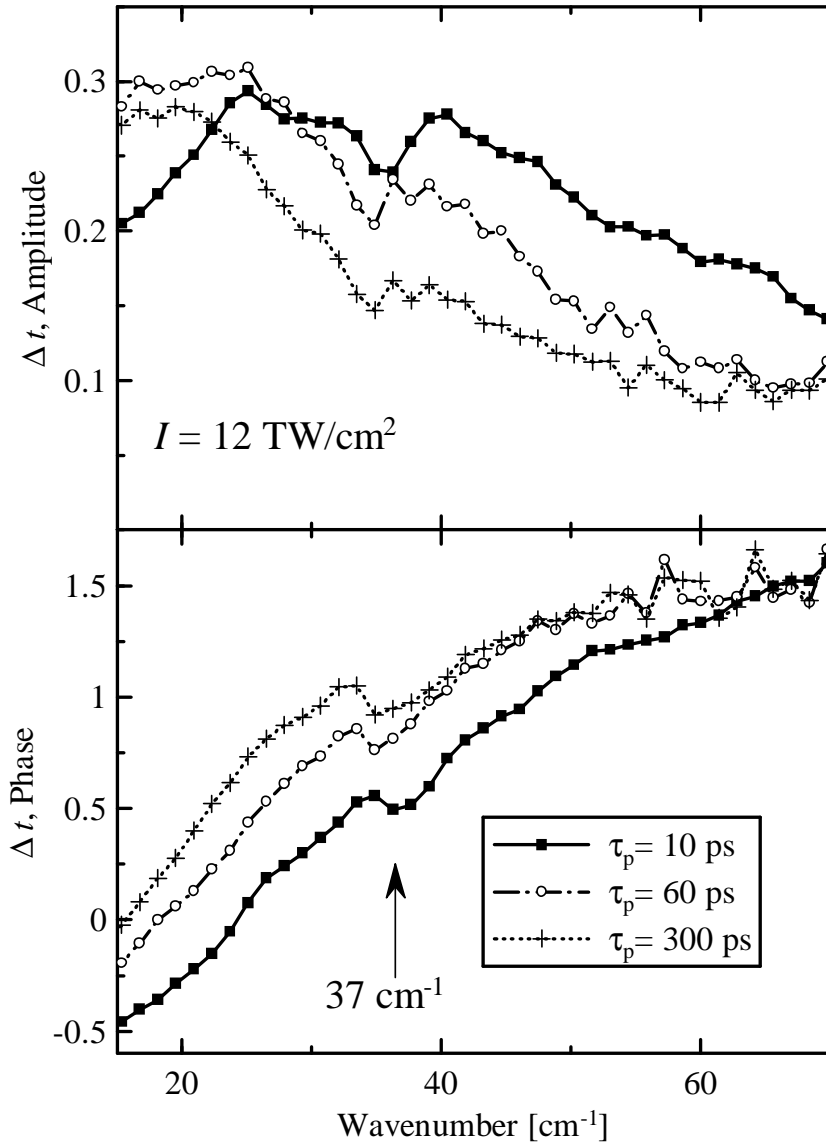


Figure 5.16: Transient transmission functions measured for different pump-probe delays. The transverse plasma oscillations can be observed at 21 cm^{-1} . The arrows show the detected transient spectral line at frequency $\approx 37 \text{ cm}^{-1}$.

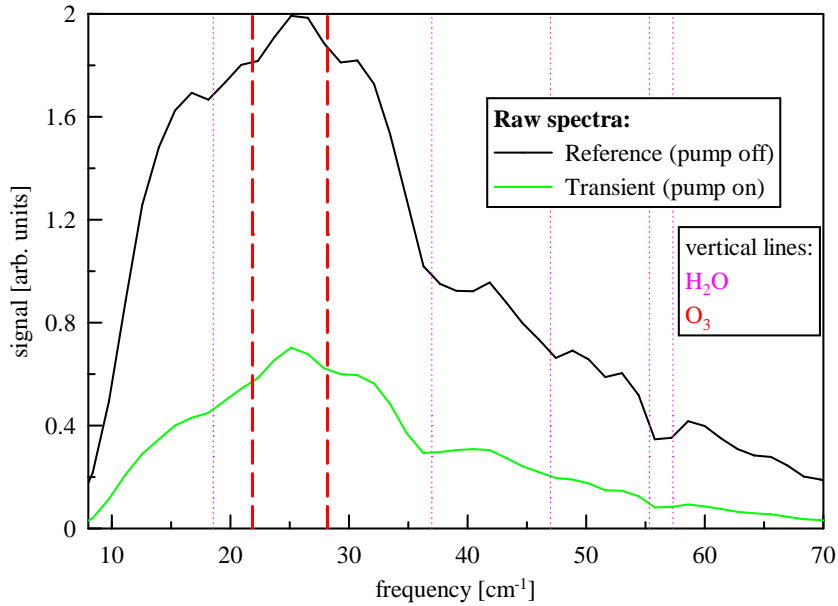


Figure 5.17: Rotational spectral lines of ozone and water in the spectrum of the transient and reference waveforms

density. Indeed, the position of this line is practically independent on the pump intensity. The evolution of the plasma contribution (i.e., the whole transmission function less the feature around 37 cm^{-1}) upon increasing the pump-probe delay is clearly marked in the spectra by a net vertical scaling of the transmission function and by significant changes of its shape below 25 cm^{-1} (Fig. 5.16). In contrast, the line at 37 cm^{-1} does not change its shape and exhibits only a very small red-shift at early times.

We have searched for a possible molecular origin of this line. Gaseous impurities, such as water vapor, could be possibly responsible for the 37 cm^{-1} spectral feature. Note that this feature is very close to a prominent water molecule rotational line. [46] Moreover, simple ab initio calculations (at the MP2/aug-cc-pvtz level) show that H_2O^+ has almost the same geometry (and thus also rotational spectrum) as H_2O and that it has about 15 % larger dipole moment than a neutral water molecule. Therefore, H_2O^+ , if formed in the experiment, would show a strong rotational line around 39 cm^{-1} . However, it is not clear, why other water lines (e.g., at about 47 cm^{-1} and 55.5 cm^{-1} , which exhibit even a stronger absorption in equilibrium water vapor transmission measurements) are not observed. [56]

As described above, ozone is formed in the chamber during the experiment. The "non-plasma" spectral feature could possibly also come from

rotation of a transient O_3^+ ion. This ion can be most likely formed via secondary ionization of ozone. The lifetime of ozone cation should be very short since it can readily neutralize by electron capture and/or react chemically. Since the geometry of O_3^+ is less bent than that of ozone (O-O-O angle of 133.6° for the former and 116.8° for the latter species) its largest rotational constant is almost twice that of O_3 (rotational constants of ozone cation evaluated at the MP2/cc-pvqz level are 6.595, 0.403, and 0.380 cm^{-1}). Ozone cation should thus exhibit strong rotational line around 31 and 43 cm^{-1} . These are the $K = 2 \rightarrow 1$ and $K = 3 \rightarrow 2$ lines within the near-prolate top approximation. [46] Our estimates are in a good agreement with the results of a most recent comprehensive study of the rotational structure in the spectra of photoionized ozone. [57] They are, however, somewhat short of a perfect match with the present experiment. [56]

Chapter 6

Summary

In this part, we summarize the results of this work. The original achievements of this thesis are:

- We applied optical pump-THz probe spectroscopy to the investigation of photoionization processes in oxygen and nitrogen. We developed a method to extract the dielectric function of the plasma from the measured THz data. This method was based on the existence of transverse oscillations of an inhomogeneous plasma in the photoionized gas. The free electron density in the plasma was determined from the position of these oscillations in the THz dielectric spectra of the plasma. We obtained electron densities in the range $10^{13} - 10^{16} \text{ cm}^{-3}$ and scattering rates of 400 and 200 ps for the plasma in oxygen and nitrogen, respectively.
- We prepared an experimental setup that enabled controlled ionization of gases: it allowed changing the wavelength, intensity and the polarization of the pump beam. Using this setup we distinguished between the mechanisms of the photoionization of the selected gases. For 810 nm pump wavelength, the strong-field tunneling mechanism was dominating in contrast with the pump at 405 nm, where the contribution of the multiphoton process was the most significant.
- We detected ozone as a product of the ionization of oxygen by its rotational spectra. We also observed a transient spectral line in the transient THz transmission spectra of oxygen active only for pump intensities higher than 12 TW/cm^2 . The origin of this feature may be in the presence of ozone cation O_3^+ , but firm evidence is still elusive.

Bibliography

- [1] D. H. Auston, K. P. Cheung, and P. R. Smith, *Appl.Phys.Lett.* **45**, 284 (1984).
- [2] R. W. Ziolkowski and J. B. Judkins, *J.Opt.Soc.Am. A* **9**, 2021 (1992).
- [3] Y. Qin, H. Guo, and S. Tang, *J. Phys.: Condens. Matter* **18**, 1613 (2006).
- [4] X.-C. Zhang, Y. Jin, and X. F. Ma, *Appl.Phys.Lett.* **61**, 2764 (1992).
- [5] X.-C. Zhang, Y. Jin, and L. J. Schowalter, *Phys.Rev.Lett.* **69**, 2303 (1992).
- [6] A. Rice, Y. Jin, X. F. Ma, X.-C. Zhang, D. Bliss, J. Larkin, and M. Alexander, *Appl.Phys.Lett.* **64**, 1324 (1994).
- [7] A. Nahata, A. S. Weling, and T. F. Heinz, *Appl.Phys.Lett.* **69**, 2321 (1996).
- [8] A. M. Sinyukov and L. M. Hayden, *Opt.Lett.* **27**, 55 (2002).
- [9] P. Y. Han, M. Tani, F. Pan, and X. C. Zhang, *Opt.Lett.* **25**, 675 (2000).
- [10] J. J. Carey, R. T. Bailey, D. Pugh, J. N. Sherwood, F. R. Cruickshank, and K. Wynne, *Appl.Phys.Lett.* **81**, 4335 (2002).
- [11] F. Kadlec, P. Kužel, and J. Coutaz, *Opt.Lett.* **29**, 2674 (2004).
- [12] F. Kadlec, P. Kužel, and J.-L. Coutaz, *Opt.Lett.* **30**, 1402 (2005).
- [13] P. R. Smith, D. H. Auston, and M. C. Nuss, *IEEE J. of Quantum Electron.* **24**, 255 (1988).
- [14] S. Kono, M. Tani, P. Gu, and K. Sakai, *Appl.Phys.Lett.* **77**, 4104 (2000).

- [15] M. Tani, K. Sakai, and H. Mimura, *Jpn.J.Appl.Phys.Lett.* **36**, 1175 (1997).
- [16] F. G. Sun, G. A. Wagoner, and X.-C. Zhang, *Appl.Phys.Lett.* **67**, 1656 (1995).
- [17] H. Němec, Master's thesis, Charles University in Prague, Faculty of Mathematics and Physics, 2002.
- [18] G. Gallot and D. Grischkowsky, *J.Opt.Soc.Am. B* **16**, 1204 (1999).
- [19] H. J. Bakker, G. C. Cho, H. Kurz, Q. Qu, and X.-C. Zhang, *J.Opt.Soc.Am. B* **15**, 1795 (1998).
- [20] P. Kužel and J. Petzelt, *Ferroelectrics* **239**, 949 (2000).
- [21] M. van Exter and D. Grischkowsky, *Appl.Phys.Lett.* **56**, 1694 (1990).
- [22] M. C. Nuss, P. M. Mankiewich, M. L. O'Malley, and E. H. Westerwick, *Phys.Rev.Lett.* **66**, 3305 (1991).
- [23] T.-I. Jeon, D. Grischkowsky, A. K. Mukherjee, and R. Menon, *Appl.Phys.Lett.* **77**, 2452 (2000).
- [24] J. T. Kindt and C. A. Schmuttenmaer, *J.Phys.Chem.* **100**, 10373 (1996).
- [25] H. Harde, N. Katzenellenbogen, and D. Grischkowsky, *J.Opt.Soc.Am.B* **11**, 1018 (1994).
- [26] R. A. Cheville and D. Grischkowsky, *Opt.Lett.* **20**, 1646 (1995).
- [27] H. Němec, F. Kadlec, and P. Kužel, *J.Chem.Phys.* **117**, 8454 (2002).
- [28] P. B. Corkum, *Phys.Rev.Lett.* **71**, 1993 (1993).
- [29] M. Lewenstein, P. Balcou, M. Y. Ivanov, A. L'Huilier, and P. B. Corkum, *Phys.Rev. A* **49**, 2117 (1994).
- [30] P. Antoine, A. L'Huilier, and M. Lewenstein, *Phys.Rev.Lett.* **77**, 1234 (1996).
- [31] I. P. Christov, M. M. Murnane, and H. C. Kapteyn, *Phys.Rev.Lett.* **78**, 1251 (1997).
- [32] I. P. Christov, M. M. Murnane, and H. C. Kapteyn, *Phys.Rev. A* **57**, R2285 (1998).

- [33] E. N. Glezer and E. Mazur, *Appl.Phys.Lett.* **71**, 882 (1997).
- [34] C. B. Schaffer, A. Brodeur, and E. Mazur, *Meas.Sci.Technol.* **12**, 1784 (2001).
- [35] R. Srinivasan and B. Braren, *Chem.Rev.* **89**, 1303 (1989).
- [36] L. J. Radziemski, *Microchem.J.* **50**, 218 (1994).
- [37] R. Rankin, C. E. Capjack, N. H. Burnett, and P. B. Corkum, *Opt.Lett.* **16**, 835 (1991).
- [38] T. Löffler, F. Jacob, and H. G. Roskos, *Appl.Phys.Lett.* **77**, 453 (2000).
- [39] D. J. Cook and R. M. Hochstrasser, *Opt.Lett.* **25**, 1210 (2000).
- [40] M. Kress, T. Löffler, S. Eden, M. Thomson, and H. G. Roskos, *Opt.Lett.* **29**, 1120 (2004).
- [41] H. Hamster, A. Sullivan, S. Gordon, W. White, and R. W. Falcone, *Phys.Rev.Lett.* **71**, 2725 (1993).
- [42] H. Hamster, A. Sullivan, S. Gordon, and R. W. Falcone, *Phys.Rev. E* **49**, 671 (1994).
- [43] S. P. Jamison, J. Shen, D. R. Jones, R. C. Issac, B. Ersfeld, D. Clark, and D. A. Jaroszynski, *J.Appl.Phys.* **93**, 4334 (2003).
- [44] L. V. Keldysh, *Sov. Phys. JETP* **20**, 1307 (1965).
- [45] J. H. Posthumus, *Rep.Prog.Phys.* **67**, 623 (2004).
- [46] G. Herzberg, *Molecular Spectra and Molecular Structure* (Van Nostrand Rheinold, New York, 1950).
- [47] S. Augst, D. D. Meyerhofer, D. Strickland, and S. L. Chin, *J.Opt.Soc.Am. B* **8**, 858 (1991).
- [48] C. Ellert and P. B. Corkum, *Phys.Rev.A* **59**, R3170 (1999).
- [49] M. J. Dewitt and R. J. Levis, *Phys.Rev.Lett.* **81**, 5101 (1998).
- [50] I. V. Litvinyuk, K. F. Lee, P. W. Dooley, D. M. Rayner, D. M. Villeneuve, and P. B. Corkum, *Phys.Rev.Lett.* **90**, 233003 (2003).
- [51] N. W. Ashcroft and N. D. Mermin, *Solid State Physics* (Holt, New York, 1976).

- [52] A. V. Benderskii, R. Zadoyan, N. Schwentner, and V. A. Apkarian, *J.Chem.Phys.* **110**, 1542 (1999).
- [53] F. F. Chen, *Introduction to Plasma Physics and Controlled Fusion. I. Plasma Physics* (Plenum, New York, 1984).
- [54] K. P. Subramanian and V. Kumar, *J.Phys. B: At.Mol.Opt.Phys.* **23**, 745 (1989).
- [55] Y. Itikawa, M. Hayashi, A. Ichimura, K. Onda, K. Sakimoto, K. Takayanagi, M. Nakamura, H. Nishimura, and T. Takayanagi, *J.Phys.Chem.Ref.Data* **15**, 985 (1986).
- [56] P. Jungwirth, private communication.
- [57] S. Willitsch, F. Innocenti, J. M. Dyke, and F. Merkt, *J. Chem. Phys.* **122**, 024311 (2005).